

1 TgLaforin, a glucan phosphatase, reveals the dynamic role of storage polysaccharides
2 in *Toxoplasma gondii* tachyzoites and bradyzoites

3

4 Robert D. Murphy^{1,2,a}, Cortni A. Troublefield^{1b#}, Joy S. Miracle^{1c#}, Lyndsay E.A. Young²,
5 Aashutosh Tripathi^{1d}, Corey O. Brizzee^{2e}, Animesh Dhara¹, Abhijit Patwardhan³, Ramon
6 C. Sun^{2fg}, Craig W. Vander Kooi^{2fg}, Matthew S. Gentry^{2fg}, Anthony P. Sinai^{1*}

7

8 Affiliations at time research was conducted:

9 1. Department of Microbiology, Immunology, and Molecular Genetics, College of
10 Medicine, University of Kentucky, Lexington, KY 40536, USA

11 2. Department of Molecular and Cellular Biochemistry, College of Medicine,
12 University of Kentucky, Lexington, KY 40536, USA

13 3. F. Joseph Halcomb III, MD. Department of Biomedical Engineering, College of
14 Engineering, University of Kentucky, Lexington KY 40506, USA

15

16 #These authors contributed equally to this work.

17 *For correspondence: Anthony P. Sinai, sinai@uky.edu

18

19 Current affiliations:

20 a. Maryland Department of Health, Laboratories Administration, Baltimore, MD
21 21205

22 b. Good Samaritan Hospital and Albert B. Chandler Medical Center Emergency
23 Departments, University of Kentucky, Lexington KY 40536

- 24 c. Department of Forestry and Natural Resources, Martin-Gatton College of
25 Agriculture, Food and Environment, University of Kentucky, Lexington, KY 40546
26 d. Department of Biochemistry, Stanford University School of Medicine, Palo Alto
27 CA 94305
28 e. Demeetra AgBio, 2277 Thunderstick Dr., Lexington, KY, USA
29 f. Department of Biochemistry and Molecular Biology, College of Medicine,
30 University of Florida, Gainesville, FL, USA
31 g. Center for Advanced Spatial Biomolecule Research, University of Florida,
32 Gainesville, FL, USA

33

34 **Running title:** TgLaforin regulation of amylopectin granules in *Toxoplasma*

35

36 **Keywords:** *Toxoplasma gondii*, amylopectin granule, glucan, reversible
37 phosphorylation, laforin, phosphatase, starch, glycogen, steady-state metabolomics,
38 glutamine

39

40 **ABSTRACT**

41 The asexual stages of *Toxoplasma gondii* are defined by the rapidly growing tachyzoite
42 during the acute infection and by the slow growing bradyzoite housed within tissue cysts
43 during the chronic infection. These stages represent unique physiological states, each
44 with distinct glucans reflecting differing metabolic needs. A defining feature of *T. gondii*
45 bradyzoites is the presence of insoluble storage glucans known as amylopectin
46 granules (AGs), the function of which remains largely unexplored during the chronic
47 infection. The presence of storage glucans has more recently been established in
48 tachyzoites, a finding corroborated by specific labeling with the anti-glycogen antibody
49 IV58B6. The *T. gondii* genome encodes activities needed for glucan turnover including:
50 a glucan phosphatase (TgLaforin; TGME49_205290) and a glucan kinase (TgGWD;
51 TGME49_214260) that catalyze a cycle of reversible glucan phosphorylation required
52 for glucan degradation by amylases. Disruption of TgLaforin in tachyzoites had no
53 impact on growth under nutrient-replete conditions. Growth of TgLaforin-KO tachyzoites
54 was however severely stunted when starved of glutamine despite being glucose replete.
55 Loss of TgLaforin attenuated acute virulence in mice and was accompanied by a lower
56 tissue cyst burden, without a direct impact on tissue cyst size. Quantification of relative
57 AG levels using AmyloQuant, an imaging based application, revealed the starch-excess
58 phenotype associated with the loss of TgLaforin is heterogeneous and linked to an
59 emerging AG cycle in bradyzoites. Excessive AG accumulation TgLaforin-KO
60 bradyzoites promoted intra-cyst bradyzoite death implicating reversible glucan
61 phosphorylation as a legitimate target for the development of new drugs against chronic
62 *T. gondii* infections.

63 **Importance**

64

65 Storage of glucose is associated with a projected need for future metabolic potential.

66 Accumulation of glucose in insoluble amylopectin granules (AG) is associated with

67 encysted forms of *Toxoplasma gondii*. AG which are not observed in rapidly growing

68 tachyzoites do appear to possess glycogen, a soluble storage glucan. Here we address

69 the role of reversible glucan phosphorylation by targeting TgLaforin, a glucan

70 phosphatase and key component of reversible glucan phosphorylation controlling AG

71 and glycogen turnover. Loss of TgLaforin fundamentally alters tachyzoite metabolism

72 making them dependent on glutamine. These changes directly impact acute virulence

73 resulting in lowering tissue cyst yields. The effects of the loss of TgLaforin on AG levels

74 in encysted bradyzoites is heterogenous, manifesting non-uniformly with the

75 progression of the chronic infection. With the loss of TgLaforin culminating with the

76 death of encysted bradyzoites, AG metabolism presents a potential target for

77 therapeutic intervention, the need for which is acute.

78

79

80

81 INTRODUCTION

82 *Toxoplasma gondii* is an opportunistic protozoan parasite of all warm-blooded animals
83 that infects one-third of humans worldwide (1, 2). Humans are primarily infected through
84 the consumption of an encysted form of the parasite: either the oocysts shed in cat
85 feces or tissue cysts found in undercooked meat from a chronically infected animal (3).

86 Encysted parasites convert into tachyzoites that rapidly divide and disseminate
87 throughout the body of the host, defining the acute phase of infection (4). Under host
88 immune pressure, tachyzoites convert into slow-growing bradyzoites that populate
89 tissue cysts which are found predominantly in the central nervous system and muscle,
90 defining the chronic phase of infection (5, 6). Tissue cysts are believed to persist for the
91 lifetime of the host and possess the ability to reactivate into tachyzoites in the context of
92 immunosuppression. Reactivation can result in the life-threatening symptoms of
93 toxoplasmosis, with toxoplasmic encephalitis being the primary condition leading to
94 mortality (7, 8). The current lack of insights into bradyzoite physiology *in vivo* precludes
95 the basic understanding needed for the development of drugs that either can clear
96 tissue cysts or target encysted bradyzoites so as to prevent reactivation (9).

97 Until recently, bradyzoites within tissue cysts were considered to be dormant,
98 metabolically inert entities. This view was challenged by our demonstration that
99 encysted bradyzoites replicate (10, 11). Moreover, bradyzoite physiology is both diverse
100 and complex as viewed through the lens of mitochondrial activity (12, 13), replication
101 status (11), and, importantly, amylopectin granule (AG) accumulation (14). Although the
102 function of AGs in bradyzoites has not been confirmed, an understanding of the roles of

103 polysaccharides elsewhere suggests that AGs are a source of energy and biosynthetic
104 potential needed for persistence, replication, reactivation, and transmission (15). These
105 assumptions remain to be tested, and thus much like bradyzoites themselves, the role
106 of AGs in the *T. gondii* lifecycle is poorly understood. Our first insights into the potential
107 relationships connecting AG to intermediate metabolism via mitochondrial and
108 replication activities have been exposed using imaging-based approaches (14).

109

110 AGs are large glucans found in the cytoplasm of bradyzoites that have classically
111 served as a morphological feature distinguishing them from tachyzoites (16-19).
112 Toxoplasma AGs are much like plant starch in that they are water-insoluble storage
113 polysaccharides composed of branched chains of glucose (18). Unlike plant starch,
114 however, AGs contain no detectable amylose (unbranched chains of glucose) (18).
115 More recently, the presence of small, punctate, cytoplasmic glucans in tachyzoites that
116 are only visible by periodic acid-Schiff (PAS) staining have been recognized (20-22),
117 and the presence of the glucan is dependent on the *T. gondii* starch synthase (TgSS;
118 TGME49_222800) (23). Like animal glycogen, this tachyzoite storage polysaccharide is
119 rapidly turned over (20), as has been observed in other protozoa (24-26), and provides
120 glucose for glycolysis (23, 27). The observation that large, insoluble glucans do not
121 accumulate within tachyzoites as they do within bradyzoites suggests that the
122 tachyzoite glucan could be a distinct and labile form of stored glucose, likely glycogen-
123 like, although its exact chemical and structural identity remains unknown.

124

125 Glucose release from starch in plants requires a cycle of direct, reversible glucan
126 phosphorylation to solubilize the starch surface, allowing access to degradation
127 enzymes such as amylases, branching enzymes, and a phosphorylase (28-30). The
128 cycle begins with the addition of phosphate directly to glucose by the glucan, water-
129 dikinase (GWD) and phospho-glucan, water dikinase (PWD) that results in the
130 unwinding of glucose chains within starch, solubilizing the starch surface (31, 32).
131 Glucose-releasing enzymes (amylases) then degrade starch until the glucan-bound
132 phosphate becomes a steric hindrance, at which point a glucan phosphatase is needed
133 to remove the phosphate and reset the cycle (33-35). *T. gondii* encodes all the activities
134 needed for glucan degradation and reversible glucan phosphorylation including the
135 glucan phosphatase, TgLaforin (TGME49_205290) (36), and glucan dikinase, *T. gondii*
136 GWD (TgGWD; TGME49_214260) (27). The central role of reversible glucan
137 phosphorylation in plants is seen in *Arabidopsis thaliana* where loss of the plant glucan
138 phosphatase, starch-excess 4 (SEX4), results in excess starch accumulation, aberrant
139 starch morphology, and severely stunted plant growth (37, Zeeman, 1998 #1387).
140 Additionally, loss of the glucan phosphatase, laforin, in humans, results in
141 hyperphosphorylated glycogen that aggregates in neurons and astrocytes causing a
142 fatal neurodegenerative childhood dementia and epilepsy (38-40). In *T. gondii*,
143 perturbations of several genes related to glucan metabolism also result in a variety of
144 similar defects including aberrant glucan accumulation, rewiring of central carbon
145 metabolism, and virulence defects in mice, highlighting the central metabolic role of
146 glucan metabolism in *T. gondii* (20-23, 27, 41-44)

147 In this study, we build on our understanding of reversible glucan phosphorylation and its
148 relevance to parasite metabolism in *T. gondii*. We have recently demonstrated that
149 TgLaforin is the glucan phosphatase in *T. gondii*, and that TgLaforin represents a
150 unique and viable drug target (36, 45, 46). Here, we investigate the role of TgLaforin
151 throughout the asexual stages by knocking out TgLaforin in Type II ME49 parasites.
152 While we expected to observe effects related to the loss of TgLaforin exclusively in
153 bradyzoites where AGs are typically observed, these effects appeared to be connected
154 to an emerging AG temporal cycle (14). More surprisingly, the loss of TgLaforin also
155 resulted in phenotypic effects in tachyzoites, also in a context-specific manner. We thus
156 established a role for TgLaforin, and by extension reversible glucan phosphorylation,
157 across both tachyzoite and bradyzoite life stages. These findings build upon previous
158 studies that increasingly demonstrate a central role for glucan metabolism throughout
159 the parasite's asexual life cycle.

160

161 **RESULTS**

162 ***T. gondii* tachyzoites contain a cytoplasmic glucan with a punctate distribution.**

163 Previous studies have presented biochemical evidence for rapid glucan turnover in *T.*
164 *gondii* Type I RH tachyzoites (20). Moreover, small granules that stain with periodic acid
165 Schiff reagent (PAS) have also been noted in the cytoplasm of tachyzoites (20, 21, 23).
166 Under acid-stress conditions, these tachyzoite glucans have been biochemically
167 characterized as pure amylopectin, and resemble AGs seen in bradyzoites (18). To
168 further characterize the nature of this tachyzoite glucan, we used multiple methods to
169 visualize them under unstressed, normal growth conditions (**Figure 1A**). PAS staining

170 confirmed that Type II ME49 tachyzoites contain small punctate granules distributed
171 throughout the cytoplasm. To determine if these PAS-stained granules in unstressed
172 tachyzoites were more glycogen- or starch-like, they were stained with IV58B6. IV58B6
173 is an anti-glycogen IgM monoclonal antibody that has previously been demonstrated to
174 be specific to glycogen (47-49) by recognizing the highly frequent branch-points found
175 in glycogen (48). Moreover, IV58B6 does not detect other glucans such as amylopectin
176 or amylose (the primary constituents of plant starch) (50). Tachyzoites stained with
177 IV58B6 in a similar pattern to PAS-stained parasites, containing small punctate granules
178 distributed throughout the cytoplasm (**Figure 1A**), suggesting that the glucan found in
179 tachyzoites is more glycogen-like than starch-like. Finally, as is well-known, *T. gondii*
180 tachyzoites contain almost no visible glucan within their cytoplasm when visualized by
181 transmission electron microscopy (TEM) (**Figure 1A**), suggesting that the glucan
182 detected by both PAS staining and IV58B6 is either water-soluble or too small to be
183 visualized, consistent with this glucan being glycogen-like.

184

185 In contrast, bradyzoites have been extensively characterized as containing starch-like
186 AGs (17-19, 51). After *in vitro* bradyzoite conversion, much of the cytoplasm stained
187 heavily with PAS (**Figure 1A**). Interestingly, IV58B6 staining intensity appeared to
188 correlate negatively with *Dolichos biflorus* agglutinin (DBA) staining intensity that
189 defines the cyst wall, implying that IV58B6 does not stain the PAS-stained glucan in
190 bradyzoites, further reinforcing the observation that structurally distinct polysaccharides
191 exist in tachyzoites and bradyzoites (**Figure 1A**). Finally, unlike in tachyzoites, AGs

192 were readily identified as electron-lucent structures throughout the cytoplasm of *in vitro*
193 generated bradyzoites by TEM (**Figure 1A**).

194

195 To verify the specificity of PAS and IV58B6 for glucose polymers, tachyzoites and
196 bradyzoites were treated with acid- α -amylglucosidase (GAA) after parasite fixation and
197 before staining. GAA cleaves both α -1,4- and α -1,6-glycosidic bonds and can therefore
198 completely digest glucans into glucose monomers. Indeed, GAA treatment resulted in
199 the disappearance of staining within both tachyzoites and *in vitro* bradyzoites (**Figure**
200 **1B**) demonstrating their specificity for glucose polymers.

201

202 ***TgLaforin colocalizes with the tachyzoite glucan***

203

204 Because *T. gondii* encodes TgLaforin, a glucan phosphatase that is more animal-like
205 than plant-like (45, 46), we reasoned that TgLaforin could be involved in the metabolism
206 of the glycogen-like glucan found in tachyzoites. To determine if TgLaforin co-localizes
207 with the tachyzoite glucan, endogenous TgLaforin was epitope-tagged with
208 hemagglutinin (HA) in *T. gondii* Type II ME49 Δ HXGPRT parasites (52) with a
209 CRISPR/Cas9 mediated strategy (**Figure 2A**) (53). Successful tagging of TgLaforin was
210 confirmed by western blotting (**Figure 2B**). Immunofluorescence analysis (IFA) of *T.*
211 *gondii* tachyzoites indicated that TgLaforin is present in small puncta throughout the
212 cytoplasm, similar to the distribution of the tachyzoite glucan (**Figure 2C**). Surprisingly,
213 TgLaforin was not detected in *in vitro* bradyzoites by IFA, 6 days post conversion
214 (**Figure 2C**). To verify that TgLaforin levels decrease during the tachyzoite to

215 bradyzoite transition, we converted *T. gondii* tachyzoites to bradyzoites in cell culture
216 using alkaline stress for 6 days and then probed the converted parasites using western
217 blot analysis. As observed using IFA, TgLaforin-HA expression decreased dramatically
218 over the course of bradyzoite differentiation (**Figure 2D**). Transcriptomic data from a
219 previous study obtained from ToxoDB.org indicates that the transcript levels for
220 TgLaforin do not substantially change over the course of differentiation, suggesting the
221 possibility that levels of TgLaforin protein are regulated by post-translational
222 mechanisms (54). To determine if TgLaforin colocalizes with the glucan present in
223 tachyzoites, we co-stained TgLaforin-HA tachyzoites with either PAS or IV58B6 along
224 with an anti-HA antibody. In tachyzoites, TgLaforin colocalized with both PAS (**Figure**
225 **2E**) and with IV58B6 (**Figure 2F**), suggesting its involvement in the metabolism of the
226 tachyzoite glucan.

227

228 ***Initial characterization of TgLaforin-KO tachyzoites***

229

230 To dissect the role of TgLaforin in *T. gondii* glucan metabolism, TgLaforin was knocked
231 out using CRISPR/Cas9 to disrupt the gene with a pyrimethamine-resistant form of the
232 dihydrofolate reductase (DHFR-TS*) under a *Neospora caninum* GRA7 (NcGRA7)
233 promoter (55) (56) (**Figure 3A**). In agreement with a genome-wide CRISPR KO screen
234 (57), TgLaforin is a non-essential gene under standard cell culture conditions, as
235 multiple TgLaforin-KO clones were successfully recovered. Integration of the DHFR-TS*
236 construct into the TgLaforin locus was verified using inside/out PCR at the chimeric
237 locus and by verifying the loss of TgLaforin transcription (**Figures 3B,C**). The TgLaforin-

238 KO line further used in this study (designated “ Δ TgLaf”) was complemented by the
239 introduction of an epitope tagged (HA) gene driven by the TgLaf promoter. The
240 complementation construct was introduced at an ectopic site in the genome that lacks
241 known coding sequences or regulatory elements on chromosome VI (**Figure S1A**),
242 while leaving the Δ TgLaf/DHFR-TS* KO lesion intact for true complementation (58).
243 This complemented strain, henceforth designated “COMP,” was successfully isolated
244 and confirmed by PCR (**Figure S1B**). Expression levels and localization were similar to
245 those seen in the TgLaf-HA line as confirmed by western blotting and IFA (**Figures**
246 **S1C-D**),

247

248 To evaluate effects of a TgLaf-KO, glucan levels in WT and Δ TgLaf tachyzoites
249 were first compared using our suite of glucan detection techniques (**Figure 3D**).
250 Surprisingly, the size and number of PAS-stained granules were not significantly
251 changed in Δ TgLaf tachyzoites relative to WT parasites. Levels of IV58B6 also
252 remained unaltered after the loss of TgLaf, and no aberrant glucan accumulation
253 was observed by TEM as has been previously reported when genes related to AG or
254 central carbon metabolism were knocked out in *T. gondii* tachyzoites (20-23, 41, 43, 44)
255 (**Figure 3D**)

256 Loss of glucan phosphatases in plants and animals results in aberrant glucan
257 accumulation, and such a phenotype was not observed within tachyzoites under
258 standard growth conditions.

259

260 ***Loss of TgLaforin results in upregulation of glutaminolysis and glutamine***
261 ***dependence in tachyzoites***

262

263 Glucan catabolism is significantly affected by the presence of covalently bound
264 phosphate, and, therefore, loss of glucan phosphatases has profound downstream
265 metabolic impacts in other systems (59, 60). We thus speculated that loss of TgLaforin
266 would result in the reduced efficiency of glucan utilization in tachyzoites and also affect
267 downstream central carbon metabolism. To test this hypothesis, we used gas
268 chromatography/mass spectrometry (GC/MS) steady-state metabolomic analysis of 3
269 μm filter-purified, syringed-passaged intracellular tachyzoites employing a previously
270 developed sample preparation technique (61).

271

272 Previously, it was demonstrated that *T. gondii* tachyzoites primarily utilize glucose and
273 glutamine to drive central carbon metabolism, synthesize macromolecules, and proceed
274 normally through the lytic cycle (62). Glucose primarily fuels glycolysis, and glutamine
275 undergoes glutaminolysis to drive the tricarboxylic acid (TCA) cycle. In the absence of
276 glucose, *T. gondii* can upregulate both glutaminolysis and gluconeogenesis to make up
277 for the loss of glucose (62, 63).

278

279 While ΔTgLaf metabolite levels remained unaltered relative to WT tachyzoites across
280 much of the TCA cycle, steady-state levels of metabolites immediately downstream of
281 glutamine were consistently more abundant in ΔTgLaf parasites compared to their WT
282 counterparts (**Figure 4A**), supporting our hypothesis that ΔTgLaf parasites were

283 deficient in glucan/glucose utilization. An increase in metabolites downstream of
284 glutamine in Δ TgLaf parasites demonstrates that Δ TgLaf parasites are possibly
285 compensating for deficiencies in glucose metabolism, supporting a role for the
286 tachyzoite glucan in intermediate *T. gondii* glucose metabolism.

287

288 To determine if loss of TgLaforin resulted in increased dependence on glutamine due to
289 impaired access to glucose, we performed plaque assays in the presence and absence
290 of glutamine (**Figure 4B**). In replete media, Δ TgLaf parasites established a similar
291 number of plaques (data not shown), indicating no defect in infectivity. Δ TgLaf plaques
292 were slightly larger than both the WT and COMP lines after 10 days of growth (**Figure**
293 **4C**). To test the effects of glutamine starvation on Δ TgLaf parasites, glutamine was
294 removed from plaque assays after parasite invasion to evaluate the effects of glutamine
295 removal on parasite growth independent of the initial invasion event. In the absence of
296 glutamine, Δ TgLaf parasites were unable to form visible plaques, whereas both the WT
297 and COMP parasites formed plaques comparable to those formed under glutamine-
298 replete conditions (**Figures 4B, C**).

299

300 ***TgLaforin is required for repeated rounds of progression through the lytic cycle***

301

302 The absence of differences in plaque number suggest that there is no specific defect in
303 infectivity. To determine which aspects of the *T. gondii* lytic cycle were impaired in the
304 absence of glutamine, the effects of glutamine starvation on initial parasite replication
305 and egress (stimulated with both A23187 (64) and zaprinast (65)) were evaluated. In

306 both assays, intracellular parasites were pre-starved of glutamine for at least 72 h
307 before assay initiation. Surprisingly, glutamine starvation had no effect on stimulated
308 egress or initial parasite replication across the three lines (**Figures S2A-C**). These data
309 demonstrate that the absence of plaques under glutamine deficient conditions cannot
310 be pinpointed to a single aspect of the Δ TgLaf lytic cycle, and that the reason for the
311 apparent absence of plaques manifested later in the infection cycle.

312

313 Plaques develop due to repeated cycles of localized infection and cell lysis resulting in the
314 clearance of infected cells over time. The absence of visible clearance prompted us to
315 examine infected host-cell monolayers for clusters of infected cells using a higher
316 magnification than is typically used in a traditional plaque assay. Low numbers of parasites
317 were seeded onto glass coverslips and fixed at 3- and 6-days post-infection, allowing for
318 visualization of developing plaques at a high magnification. In these experiments, glutamine-
319 depleted host cells were pre-starved of glutamine prior to infection with parasites to allow for
320 potential for invasion defects. Importantly, Δ TgLaf parasites demonstrated similar infectivity to
321 WT parasites under both glutamine-replete and depleted conditions, indicating no gross initial
322 invasion defect. After 3 days of growth, no statistical differences of nascent plaque sizes were
323 noted between glutamine-replete and starved conditions in both the WT and COMP lines.

324 However, Δ TgLaf parasites in glutamine starved conditions were already 1.5x smaller in area
325 than their counterparts in replete conditions (**Figure 4D**). By day 6 of growth, this difference
326 had widened to a >3x difference between glutamine replete/depleted Δ TgLaf parasites (**Figure**
327 **4E**). Such a difference was not detected between the two conditions in WT/COMP parasite
328 lines. By measuring the internal clearing area relative to the total plaque perimeter, it was also

329 noted that Δ TgLaf parasites were much less capable of forming clearings than the WT/COMP
330 lines (**Figures S2D, E**), rather they formed clusters of infected cells akin to “turbid plaques”
331 (66, 67) due to their presumed inability to compete with host cell growth, as the infection
332 progressed. This observation explains the apparent absence of plaques seen at the lower
333 magnification used in traditional plaque assays (**Figure 4B**). The modified plaque assay
334 therefore confirmed that the loss of TgLaforin penalized the summation of repeated rounds of
335 the energy-demanding lytic cycle rather than one particular aspect of the lytic cycle.
336 Representative images from this assay can be found in **Figure S2D**.

337

338 ***Loss of TgLaforin results in aberrant bradyzoite AGs in vitro***

339

340 To determine if loss of TgLaforin resulted in bradyzoite conversion defects, or aberrant
341 AG accumulation, parasites were converted to bradyzoites *in vitro* using alkaline stress.
342 During differentiation, the parasitophorous vacuole membrane (PVM), delimiting the
343 replicative niche established by tachyzoites, converts into the cyst wall that surrounds
344 bradyzoites within their host cell (68, 69). The cyst wall is heavily glycosylated and
345 contains N-acetylgalactosamine (Gal-NAc) that is detectible with Dolichos biflorus
346 agglutinin (DBA) (68). Using DBA-FITC intensity as a marker for differentiation, no
347 penalty was imposed by the loss of TgLaforin on cyst wall formation over the course of
348 six days (**Figure 5A**). Somewhat surprisingly, Δ TgLaf mutant parasites tended to exhibit
349 stronger labeling with DBA at day 6. We additionally assessed the levels of
350 accumulated glucans using PAS staining (**Figure 5B**). Semi-quantitative analysis of
351 PAS intensity within vacuoles during stage conversion showed an expected increase

352 over time, but no significant difference between the WT and Δ TgLaf parasites was
353 detected over the time course examined.

354

355 Because PAS is not specific to glucans and can stain other glucose-containing
356 molecules such as glycosylated protein and provides no resolution on glucan
357 morphology, we utilized TEM to gain higher resolution on AG formation during
358 bradyzoite differentiation. After 6 days of conversion, WT parasites produced AGs that
359 were circular/ovoid and white (**Figure 5C**). In contrast, Δ TgLaf parasites contained
360 irregular AGs that were morphologically distinct from AGs that were observed in WT
361 parasites (**Figure 5C**). AGs in Δ TgLaf parasites appeared amorphous and grayer, while
362 appearing to occupy more area of the parasite cytoplasm compared to WT parasites. To
363 quantify this phenotype, the area of AGs was calculated relative to total parasite area to
364 determine the percentage of the parasite body occupied by AGs in both WT and Δ TgLaf
365 strains (**Figure 5D**). Strikingly, AGs occupied approximately 4x more relative area in
366 Δ TgLaf parasites when compared to WT, indicating that PAS staining may lack the
367 sensitivity to capture this difference, in tissue culture generated bradyzoites. When
368 analyzed on an 8-bit gray scale, AGs in Δ TgLaf parasites were significantly grayer
369 (grayscale 0-255 is black-white) than those found in WT parasites, highlighting potential
370 chemical differences (such as predicted hyperphosphorylation) resulted in differential
371 interactions of Δ TgLaf AGs with the TEM contrast reagents, likely the heavy metals
372 used in processing (**Figure 5E**).

373

374 Examination and quantification of AGs in the COMP line revealed that complementation
375 of TgLaforin restored most of the circular/ovoid AG cross sections while they also
376 occupied less space in the cytoplasm and were overall more like those found in WT
377 parasites (**Figures 5C-E**). Thus, cell culture experiments demonstrate that the loss of
378 TgLaforin presents itself in both a context and life cycle stage-specific manner.

379

380 ***Loss of TgLaforin results in attenuated virulence and cyst formation in vivo***

381

382 We hypothesized that loss of TgLaforin may impose a steep penalty under the stresses
383 and potential nutrient scarcities encountered *in vivo* as it does when nutrients (such as
384 glutamine) are scarce *in vitro*. To test this hypothesis, equal numbers of male and
385 female CBA/J mice were infected with 100 tachyzoites intraperitoneally (i.p.) and
386 monitored daily using a previously developed five-stage body index score to track the
387 severity of symptoms associated with a tachyzoite infection over the course of 28 days
388 (52).

389

390 Mice infected with WT parasites began demonstrating symptoms of infection ten days
391 after infection with tachyzoites (**Figure 6A**). However, mice infected with Δ TgLaf
392 parasites did not begin to exhibit symptoms until 15 days after infection. Moreover, mice
393 that became symptomatic from WT parasite infections often proceeded through all
394 stages of symptomology, and only a minor proportion of mice that became sick were
395 able to recover from infection (>70% of mice became moribund or died). Infection from
396 Δ TgLaf parasites, however, resulted in the majority of mice only developing mild

397 symptoms (Stage 2 or less) with many of these mice recovering (**Figure 6A**). The
398 attenuated capacity of the Δ TgLaf parasites to cause symptoms in mice was reflected in
399 the mortality rates of the infected mice: infection with WT parasites resulted in 73%
400 mortality rate after 28 days whereas Δ TgLaf parasites only caused 17% mortality
401 (**Figure 6B**). Complementation of TgLaforin partially rescued this defect in virulence as
402 COMP parasites resulted in an earlier onset of symptomatic infection at Day 11, and the
403 majority (53%) of mice succumbed to infection during the first 28 days (**Figures 6A, B**).

404
405 Because the acute phase of infection was significantly attenuated by the loss of
406 TgLaforin, we hypothesized that cyst numbers would be significantly lowered. To
407 determine the number of cysts formed after 28 days of acute infection (Week 4), we
408 used a previously established protocol for harvesting and counting tissue cysts from
409 infected mouse brains, following purification on Percoll gradients (11, 70). Consistent
410 with the ability of Δ TgLaf parasites to stage convert in culture, mutant parasites were
411 able to establish tissue cysts *in vivo*. However, the number of cysts recovered from
412 Δ TgLaf infected animals was lower than those obtained from WT infected animals
413 (**Figure 6C**). Restoration of TgLaforin in the COMP line effectively restored tissue cyst
414 yields.

415

416 ***Δ TgLaf tissue cysts can reestablish infections in naïve mice***

417

418 To determine if the loss of TgLaforin impacted the overall viability/infectivity of *in vivo*
419 tissue cysts, we examined the disease progression in WT, Δ TgLaf, and COMP infected

420 animals following injection of 20 tissue cysts i.p. Consistent with prior data (52),
421 infection with tissue cysts results in markedly lower pathology and consequent mortality
422 during the acute phase for WT as well as both the Δ TgLaf and COMP lines (**Figure 7A,**
423 **B**). Mortality from cyst infections did not differ statistically among the three lines (**Figure**
424 **7A, B**). Twenty-eight days post-infection, cyst burdens were again enumerated for each
425 line. Δ TgLaf parasites were once again much less competent at forming cysts *in vivo*
426 (**Figure 7C**). However, unlike the tachyzoite infection, the COMP line was unable to
427 rescue this defect in cyst formation (**Figure 7C**), suggesting that physiological and
428 metabolic changes associated with the loss of TgLafarin manifest differently based on
429 the life cycle stage, impacting their capacity to be complemented.

430

431 ***Loss of TgLafarin results in a delayed starch-excess phenotype within encysted***
432 ***bradyzoites***

433 We leveraged the inherent fluorescence of PAS coupled with an optimized labeling
434 protocol to determine the mean intensity of WT, Δ TgLaf and complemented (COMP)
435 tissue cyst using Image J (**Figure. 8A**). Similar to the pattern observed with *in vitro*
436 generated bradyzoites (**Figure. 5**), *in vivo* derived tissue cysts harvested at 28 days
437 (Week 4) post infection failed to demonstrate a starch-excess phenotype in the Δ TgLaf
438 mutant (**Figure 8A**). Notable here, is the fact that at week 4 post infection, bradyzoites
439 are in a state of low AG accumulation (14), and presumably, low turnover, potentially
440 minimizing the impact of the loss of TgLaf. Our prior data indicate that tissue cysts
441 harvested at week 6 post infection are in markedly more dynamic state noted by
442 increased accumulation of AG, higher levels of active mitochondria and increased

443 replicative activity (14). Quantification of mean PAS intensity exposed a dramatic
444 increase in AG levels comparing WT and Δ TgLaf tissue cysts, with overall levels
445 between WT and COMP cysts remaining not significantly different (**Figure 8A**). This
446 points to the effect of the loss of TgLaf demonstrating a delayed starch excess
447 phenotype, indicating the penetrance of the mutation is potentially connected to
448 achieving a threshold level of AG as a part of an emerging AG cycle (14).

449 The development of AmyloQuant, an imaging-based application, permits the direct
450 measurement of relative AG levels within tissue cysts (14). With is application,
451 individual PAS-labeled pixels are classified into 4 bins defining background pixels
452 (black: 0-10 grayscale), low intensity (blue: 10-25), intermediate (green: 25-50) and high
453 (red: > 50 grayscale). Thirty randomly acquired tissue cysts, (the mean intensity of
454 which were reported in **Figure 8A**) from WT, Δ TgLaf and COMP mice infected for 4
455 weeks (**Figure 8B, top row**) and 6 weeks (**Figure 8B, bottom row**) are arrayed based
456 on their overall mean intensity. The percentage of pixels within each of the 4 bins is
457 presented as a stacked plot, with the AmyloQuant generated thumbnails representing
458 spatial heatmaps of AG intensity at 5 cyst intervals as presented below each stacked
459 plot. This analysis reveals that despite the mean PAS intensities not being statistically
460 significant (**Figure 8A**), several Δ TgLaf cysts present with varying levels of high
461 intensity (red) PAS labeling. Notable here is that with this cohort of cysts, effective
462 complementation of AG levels is not observed.

463 As expected for wild type Week 6 tissue cysts (14), markedly increased AG
464 accumulation is evident compared to Week 4 cysts (**Figure 8B**). This phenotype is
465 grossly exaggerated in the case of Δ TgLaf tissue cysts (**Figure 8B**), displaying the

466 expected starch excess phenotype. Even so, not all Δ TgLaf cysts present uniformly
467 high levels AG based on PAS intensity (**Figure 8B**). Notable here, the levels and
468 distribution of AG levels within the COMP line appear to be intermediate to that
469 observed for the WT and Δ TgLaf, pointing to the plasticity of the phenotype.
470 Several recent studies targeting activities connected with AG metabolism report
471 differences in cyst yield as well as cyst size (21-23, 41). We therefore examined if the
472 loss of TgLaf resulted in any significant impact of cyst size. Contrary to other reports
473 however no differences in cyst diameter were noted for either week 4 or week 6
474 harvested tissue cysts (**Figure S3A**). Furthermore, we found no strong correlation
475 between cyst size and mean AG levels as defined by PAS labeling intensity (**Figure**
476 **S3B**).

477

478 **Aberrant AG accumulation in Δ TgLaf tissue cysts promotes bradyzoite death.**

479 The inherent harshness of PAS labeling causes differential labeling intensity related
480 issues with regard to the labeling of bradyzoite nuclei (14) as well as labeling for
481 TgIMC3 a marker of recent replication (14). As a result, the relationship between AG
482 levels and replication associated outputs (packing density and recency of replication)
483 could not be reliably implemented in the context of the TgLaf mutant. We therefore
484 resorted to the direct examination of purified tissue cysts by transmission electron
485 microscopy.

486 We adapted a protocol designed to capture and image low abundance cells by TEM by
487 making it compatible with our tissue cyst purification protocol (see Methods) (71, 72).

488 TEM imaging revealed that while WT parasites formed largely normal/canonical AGs *in*

489 *vivo* as seen *in vitro* (**Figure 9** [compare with **Figure 5A**]), Δ TgLaf parasites contained
490 almost exclusively aberrant AGs that mirrored the same morphological defects seen *in*
491 *vitro* (**Figure 9** and **Figure S4**). Δ TgLaf AGs were irregularly sharpened with a flat,
492 multi-lobed appearance. Importantly, COMP parasites neither over-accumulated nor
493 formed aberrant AGs, demonstrating that this defect is specific to loss of TgLaforin
494 (**Figure 9**).

495
496 In addition to containing aberrant AGs, the internal morphology of Δ TgLaf parasites
497 appeared to be altered by the presence of the AGs, as significant organelle
498 displacement was also noted (**Figure 9, S4**). Many of the Δ TgLaf parasites also
499 appeared hollow or “ghost-like” in appearance resulting from their unstained/absent
500 cytoplasm, which included the apparent loss of the nucleus in several bradyzoites
501 (**Figure 9, S4**). These data suggest that a significant number of the Δ TgLaf bradyzoites
502 were inviable within the cyst (**Figure 9, S4**). Together, these direct and selective
503 impacts of TgLaforin’s loss on both bradyzoite viability and growth *in vivo* establish
504 TgLaforin as a potentially druggable target.

505

506 **DISCUSSION**

507

508 The asexual life cycle of *Toxoplasma gondii* is defined by two fundamentally distinct
509 forms: the rapidly replicating tachyzoite and the slowly growing bradyzoite. These forms
510 represent distinct physiological states that can be further subdivided, particularly within
511 encysted bradyzoites (73). Insights into these physiological states, inferred from

512 transcriptomic analyses, are reinforced in emerging metabolomic studies (74, 75). In
513 these studies, glucose and glutamine, which are both linked to energetics, biosynthesis,
514 and intermediary metabolism, appear as critical metabolites. Importantly, glucose can
515 be stored in polymers like glycogen and amylopectin during times of low energy need.
516 Stored glucose can be present in an accessible and labile form for rapid mobilization
517 such as glycogen, or in a less soluble forms as AGs from which it can be accessed
518 more slowly (76, 77). Reversible glucan phosphorylation facilitates the breakdown of
519 such glucan polymers by disrupting the crystalline helices on the glucan surface (78). *T.*
520 *gondii* encodes the capacity for reversible glucan phosphorylation (27, 36, 45, 46). The
521 contribution of this process to tachyzoite and bradyzoite biology was evaluated through
522 targeted manipulation of the glucan phosphatase, TgLaforin (36).

523

524 The accumulation of AGs within bradyzoites and their apparent absence in tachyzoites
525 has been used as discriminator between these life cycle stages (16, 79). Detailed
526 examination, however, presents a considerably more nuanced picture, alongside
527 emerging evidence that points to rapid glucan turnover within tachyzoites (20). In the
528 current study, using an IgM monoclonal antibody (IV58B6) that specifically recognizes
529 glycogen-like glucose polymers (47, 48), we demonstrate that the stored glucan within
530 tachyzoites is structurally closer to animal glycogen (47, 48) than the insoluble plant-like
531 AG granules found in bradyzoites (17, 19). This duality between life stages may be
532 additionally reflected in the observation that TgLaforin, the glucan phosphatase, and
533 TgGWD (TGME49_214260), the partner kinase that is predicted to phosphorylate *T.*
534 *gondii* glucan polymers, trace their structural lineages to animals and plants,

535 respectively (45, 46). The glycogen-like glucan polymer appears to be specific to
536 tachyzoites as its levels decrease upon *in vitro* differentiation while the overall PAS
537 intensity increases (**Figure 1A**). This suggests that the tachyzoite glucan and bradyzoite
538 AG are architecturally distinct polymers with respect to both branching frequency,
539 solubility, and phosphorylation status (**Figure 2D**). The glucose-based nature of both
540 particles is supported by the elimination of both IV58B6 and PAS staining with α -
541 amyloglucosidase treatment (**Figure 1B**).

542

543 To address the contribution of stored glucans in both tachyzoites and bradyzoites, we
544 disrupted the glucan phosphatase TgLaforin. This enzyme preferentially removes
545 phosphate groups from the C3 carbon on glucose facilitating access to enzymes that
546 release glucose (36). The loss of other glucan phosphatases such as SEX4 in *A.*
547 *thaliana* and laforin in mammals is accompanied by excessive accumulation of aberrant
548 starch and hyperphosphorylated glycogen in plants and animals (37, 39, 40, 80, 81).
549 Surprisingly, given these penalties in other systems, Δ TgLaf tachyzoites exhibited no
550 gross morphological changes in glucan content, consistent with a recent study in which
551 TgGWD was knocked out (27). These observations contrasts with other KO studies of
552 glucan pathway associated proteins such as CDPK2 (20), glycogen phosphorylase (41),
553 the PP2A holoenzyme (44), and α -amylase (22) which all reported exaggerated glucan
554 accumulation in tachyzoites.

555 Despite the absence of glucan accumulation in Δ TgLaf tachyzoites, the loss of this gene
556 exerts an effect on tachyzoite glucan metabolism. Consistent with the metabolic defects
557 associated with the loss of laforin in humans (60), loss of TgLaforin in *T. gondii* resulted

558 in altered central carbon metabolism that manifested as Δ TgLaf parasites' dependence
559 on glutamine (**Figure 4, S2D,E**). Δ TgLaf tachyzoite dependence on glutamine supports
560 recent studies demonstrating that tachyzoites utilize storage glucans for glucose
561 allocation (23) because the presumed loss of efficient glucan degradation results in
562 tachyzoite dependence on glutamine (**Figures 4B,C**). As *T. gondii* tachyzoites primarily
563 utilize glucose and glutamine to support their rapid growth, this dependence on
564 glutamine reinforces previous observations that glutamine can substitute for glucose in
565 this altered metabolic landscape (62, 82). These results are consistent with many
566 previous studies that disrupt glucose and/or glucan metabolism, but contrast with
567 others. Disruption of TgGT1 (TGME49_214320), the only plasma-membrane glucose
568 transporter in *T. gondii* (62, 83), or TgHK (TGME49_265450), the *T. gondii* hexokinase,
569 resulted in upregulation of gluconeogenesis, and parasite growth was highly attenuated
570 with glutamine depletion (82). Most strikingly, parasites lacking starch synthase (TgSS;
571 TGME49_222800) displayed no dependence on glutamine and, in fact, grew faster than
572 WT parasites when both glucose and glutamine were removed from the culture media
573 (23). Interestingly, however loss of TgSS did result in lower glucose flux through
574 glycolysis (23), consistent with our findings that demonstrate a role for the tachyzoite
575 glucan in glucose allocation. This finding may suggest that while the absence of AG in
576 the Δ TgSS parasites may not be detrimental, overaccumulation as observed in Δ TgLaf
577 cysts can contribute to toxicity (**Figure 9**). Perturbations of other glycolytic enzymes
578 also demonstrated varied effects related to the presence of glutamine: loss of the
579 glycolytic enzyme glyceraldehyde-3-phosphate dehydrogenase (GAPDH1) could be
580 rescued with high levels of glutamine (84) (84), but glutamine could not rescue pyruvate

581 kinase (TgPYK1) knockdown parasites (85). Our data indicate that loss of access to key
582 nutrients such as glucose and glutamine has a profound impact on the repeated rounds
583 of the lytic cycle without being attributable to one specific process within the cycle,
584 suggesting that the penetrance of the phenotypic defect manifests cumulatively over
585 time, rather than being hard wired in each infection cycle (**Figures 4D,E, S2D,E**).

586
587 Despite glucan metabolism being historically viewed as being important in the chronic
588 infection, TgLaforin protein expression decreased during the tachyzoite to bradyzoite
589 conversion *in vitro* even though its transcript levels do not change (**Figures 2C,D**). This
590 could be a transient observation as the downregulation of glucan catabolism during
591 conversion would facilitate accumulation of AGs for the chronic infection. We therefore
592 examined how the loss of TgLaforin affected the capacity of Δ TgLaf parasites to
593 differentiate *in vitro*. The Δ TgLaf parasites exhibited no defect in AG-accumulation
594 kinetics, detected by PAS staining, or in cyst wall formation, detected with DBA lectin
595 over the course of the *in vitro* conversion assay (**Figure 5A, B**). The lack of difference in
596 PAS labeling between both the WT and the Δ TgLaf lines, however, did not reveal the
597 differences noted by TEM (**Figure 5C-E**). As initially hypothesized would be the case in
598 both tachyzoites and bradyzoites, loss of TgLaforin resulted in aberrant AG
599 accumulation within *in vitro* bradyzoites that is marked by changes in both level and
600 morphology (**Figures 5C-E**), as seen in plants and vertebrates (37-40, 81). AGs in the
601 Δ TgLaf parasites were not only present at higher levels but were potentially chemically
602 distinct considering their differential binding to TEM contrast metals (**Figure 5E**). Given
603 that TgLaforin is a confirmed glucan phosphatase (36), we speculate that AG

604 hyperphosphorylation may account for both altered morphology and appearance by
605 TEM.

606

607 These context-specific phenotypes suggested that the Δ TgLaf mutant would manifest
608 phenotypic differences in both the acute and chronic phases on infection *in vivo*.
609 Indeed, the loss of TgLaforin was associated with a markedly reduced symptomology
610 and associated mortality compared to both the parental and complemented parasites
611 during acute tachyzoite-initiated infection (**Figures 6A,B**). Not only was there a delay in
612 symptomatic disease, but also a reduction in disease severity and overall cyst burden.
613 Symptomology in the acute infection is driven by an increasing parasite burden driving
614 an overexuberant host inflammatory response (4, 86). The delayed symptom onset
615 suggests growth inhibition by the stringent *in vivo* environment that more effectively
616 controls Δ TgLaf parasite infection with less robust inflammation. Notably, the delayed
617 and milder course of the tachyzoite infection resulted in a lower overall cyst burden in
618 surviving animals compared to infection with both WT and COMP parasites (**Figure**
619 **6C**).

620 Infection with Δ TgLaf tachyzoites resulted in fewer tissue cysts being generated relative
621 to WT and COMP parasite (**Figure 6C**) The basis for this is not clear, but suggestive of
622 a regulatory imbalance that is masked in tachyzoites but evident in tissue cyst-initiated
623 infections which have the additional burden of converting from bradyzoites to
624 tachyzoites, surviving the chronic infection before forming new tissue cysts. This could
625 potentially parallel the observations with plaque formation *in vitro* (**Figure 4, S2**).

626 Our ability to quantify and map relative AG levels within tissue cysts using
627 AmyloQuant (14), confirm that the loss of TgLaf does not fundamentally alter the
628 initiation and early progression of an AG cycle as evidenced by the effect of the
629 mutation not being evident in Week 4 tissue cyst in the form of the expected starch
630 excess phenotype (**Figure 8**). The effect of the Δ TgLaf mutation becomes evident in
631 week 6 tissue cysts where a massive increase in AG accumulation (**Figure 8**) is likely
632 due to an imbalance caused by the predicted defect in AG turnover. As with other
633 phenotypes associated with this mutation, the effect continues to exhibit phenotypic
634 variation noted by roughly a third of the imaged cysts lacking a significant proportion of
635 high intensity pixels (red), while others are completely oversaturated (**Figure 8**). These
636 distinct populations are not reflected in any way based on the size of the cyst (**Figure**
637 **S3**). In fact, contrary to other reports regarding AG metabolism associated genes, the
638 TgLaf mutation has no significant effect on tissue cyst size (**Figure S3**).

639 While we were not able to accurately quantify either the nuclear number or TgIMC3
640 intensity distributions as markers of packing density and replicative activity in PAS
641 stained tissue cysts (14), TEM analysis exposed the true consequence of the loss of
642 TgLaf within tissue cysts in vivo (**Figure 9, S4**). Wild type tissue cysts presented with
643 clusters of small amylopectin granules as well as evidence of active endodyogeny
644 (**Figure 9**). In contrast Δ TgLaf cysts presented bradyzoites laden with AG to the point
645 where other organellar structures were obscured (**Figure 9, S4**). Several bradyzoites
646 lacked nuclei while others lacked the cytoplasm (**Figure 9, S4**). Together, these
647 features are incompatible with viability. The presence of such features does not apply to
648 all bradyzoites within the cyst accounting for the fact that these cysts are able to initiate

649 a new infection (**Figure 7.**), albeit with lower virulence and cystogenic potential. These
650 finding suggest that AG metabolism is under tight control as dysregulated accumulation
651 can result in cumulative defects resulting in toxicity and death. The high frequency of
652 these abnormal parasites suggests that reversible glucan phosphorylation and
653 TgLaforin specifically represent legitimate bradyzoite specific drug targets. We recently
654 described a small molecule that inhibits recombinant TgLaforin (36) which serves as a
655 potential starting point in the development of a new class of anti-*Toxoplasma*
656 therapeutic agents. Particularly exciting in this context is the fact that a class of drugs
657 exhibiting efficacy with tissue cyst clearance (atovaquone (87, 88) endochin-like
658 quinolones (89-91) and JAG21 (92)), all target mitochondrial respiration. When glucose
659 is limiting, mitochondrial respiration can be driven by glutamine. This provides an
660 opportunity for combination therapy to promote the clearance of toxoplasma tissue cysts
661 as a means of mitigating the risk of reactivation.

662

663 **METHODS**

664

665 ***Fibroblast and parasite culture and maintenance***

666

667 All parasite lines were maintained in human foreskin fibroblasts (HFFs; ATCC) in
668 Minimal Essential Media- α (MEM- α ; Gibco) supplemented with 7% heat-inactivated fetal
669 bovine serum (FBS; Gemini Bio), 100 U/mL penicillin, 100 μ g/mL streptomycin, and an
670 additional 2 mM L-glutamine (Gibco; 4 mM total L-glutamine). Cells and parasites were
671 incubated at 37°C and 5% CO₂ in a humidified incubator. Genetically modified parasites

672 were maintained in MEM- α containing 7% dialyzed FBS (Gemini Bio) and either
673 pyrimethamine (1 μ M), mycophenolic acid/xanthine (MPA: 25 μ g/mL, xanthine: 50
674 μ g/mL), or 6-thioxanthine (6-Tx: 80 μ g/mL).

675

676 Assays analyzing the effects of glutamine deprivation used Dulbecco's Modified Eagle
677 Medium (DMEM). Both glutamine-replete (Gibco, 11966025) and depleted (Gibco,
678 11054020) DMEM were supplemented with 7% dialyzed FBS. Glutamine-replete media
679 from the supplier lacked other key nutrients and was modified to contain 5 mM glucose,
680 1 mM sodium pyruvate, and 4 mM L-glutamine.

681

682 ***Generation of T. gondii mutant lines***

683

684 *Type II ME49 Δ HXGPRT* ("WT"—the parental line utilized to generate all other lines in
685 this study): This line was generated in a previous study using CRISPR/Cas9 targeting of
686 TgHXGPRT and selection with 6-Thioxanthine (52).

687 *TgLaforin-3xHA-HXGPRT*: TgLaforin was epitope tagged with HA at the C-terminus
688 using CRISPR-Cas9 to disrupt the TgLaforin 3'UTR immediately downstream of the
689 endogenous stop codon as has been previously described (53). Briefly, a sgRNA
690 immediately downstream of the TgLaforin stop codon was designed using the
691 EuPaGDT design tool (<http://grna.ctegd.uga.edu>). The top hit was selected (**Table S1**)
692 and used to replace the sgRNA sequence in pSAG1::CAS9-U6::sgUPRT, a plasmid
693 containing both Cas9-green fluorescent protein (GFP) and an interchangeable sgRNA
694 scaffold (56); (**Table S2**). Replacement of the interchangeable sgRNA was

695 accomplished using a Q5 site-directed mutagenesis kit (**Table S3**) (New England
696 BioLabs). The TgLaforin-HA tagging construct was generated by amplifying the 3' end
697 of the TgLaforin-HA construct generated for complementation (see generation of COMP
698 line below and **Tables S2 and S3**) along with the connected HXGPRT selectable
699 marker. Both the TgLaforin-HA PCR-amplicon and the CRISPR-Cas9-GFP were
700 transfected into 1.4×10^7 *T. gondii* ME49 Δ HXGPRT parasites (2:1 insert:plasmid molar
701 ratio; 30 μ g DNA total) by electroporation with a time constant between 0.16 and 0.20
702 msec (BioRad Gene Pulser II). After 24 h, surviving parasites were syringe-passaged
703 from infected HFFs with a 27 G needle to lyse host cells, and gravity-filtered through a
704 10 μ m filter to remove host-cell debris. Successful transformants were then enriched by
705 use of fluorescence-activated cell sorting (FACS; Sony SY3200, installed in a biosafety
706 level II cabinet) to select parasites expressing Cas9-GFP from the transfected plasmid
707 by isolating GFP+ parasites. HFFs were infected with GFP+ parasites, and then placed
708 in media containing MPA/xanthine 24 h later to select for restoration of HXGPRT.
709 MPA/xanthine-resistant parasites were cloned by limiting dilution into a 96 well plate.
710 Wells containing single plaques were picked 7 days later and expanded. Genomic DNA
711 was extracted from clones using a Proteinase K treatment detailed elsewhere (93).
712 Successful tagging of TgLaforin was verified using sequencing, immunoblotting, and
713 IFA.

714 *ME49 Δ HX Δ TgLaforin* (“ Δ TgLaf”): TgLaforin was disrupted using a CRISPR-Cas9
715 mediated strategy as detailed above, with several differences. Briefly, a single sgRNA
716 was designed to target the first exon of TgLaforin with the top hit from EuPaGDT (**Table**
717 **S1**). To disrupt TgLaforin with a selectable drug marker, DHFR-TS*, a pyrimethamine-

718 resistant mutant of the DHFR gene, containing a 5'-NcGra7 promotor and DHFR 3'UTR
719 was amplified from pJET-NcGra7_DHFR (**Table S2**). Amplification utilized primers
720 containing 40 nt extensions homologous to the 5'- and 3'-UTR of TgLaforin to
721 encourage homologous recombination-mediated whole-gene replacement with the drug
722 cassette (**Table S3**). Both the PCR-amplified DHFR* homology cassette and the
723 CRISPR-Cas-GFP plasmid were transfected and FACS-sorted as described above.
724 GFP+ parasites underwent drug selection in pyrimethamine. Parasites were then cloned
725 and expanded as detailed above. Successful integration of the DHFR* cassette into the
726 TgLaforin locus was verified using PCR with inside/out primer pairs to the chimeric,
727 interrupted gene (**Table S3**). Loss of TgLaforin transcription was verified by purifying
728 RNA from TgLaforin clones on RNeasy spin columns (Qiagen). Using the Promega
729 Reverse Transcriptase System, cDNA was synthesized from RNA extracts. Primers
730 designed for full-length TgLaforin amplification were then used to verify loss of
731 TgLaforin cDNA in knockout lines.

732 *ME49ΔHXΔTgLaforin+ChrVI-TgLaforin* ("COMP"): Complementation of TgLaforin was
733 also executed using a CRISPR-mediated strategy. A sgRNA to a neutral locus on
734 chromosome VI identified previously (58) was generated using the same mutagenesis
735 strategy as above (**Table S1 and S3**). A full length TgLaforin cDNA containing its
736 endogenous 5'UTR (2000 bp upstream from gDNA) was synthesized by GenScript and
737 inserted into a pHA3x-LIC vector (**Table S2**) containing a C-terminal HA tag and a
738 DHFR 3'UTR, linked to the HXGPRT selectable marker (named "TgLaforin-HA3x-LIC";
739 also used above for endogenous tagging to create the TgLaforin-HA line). The entire
740 construct (5'UTR:TgLaforin-cDNA:DHFR-3'UTR:HXGPRT) was amplified from the

741 vector and co-transfected into Δ TgLaf parasites with the CRISPR-Cas9 plasmid as done
742 above. Successful transformants that received the HXGPRT marker were selected with
743 MPA/xanthine. Successful insertion of TgLaforin along with its promoter was verified
744 using PCR (**Table S3**), immunoblotting, and IFA with an anti-HA antibody (Abcam).

745

746 ***Immunofluorescence (IF) staining***

747

748 HFFs were grown on glass coverslips until confluent and subsequently infected.
749 Infected HFFs were fixed with either methanol (MeOH) (100%, -20°C) or methanol-free
750 paraformaldehyde (PFA) (4% in phosphate-buffered saline (PBS); Electron Microscopy
751 Sciences) as indicated below for each antibody. Infected HFFs fixed with PFA were
752 permeabilized in 0.1% TritonX-100 in PBS++ (PBS containing 0.5 mM CaCl₂ and 0.5
753 mM MgCl₂) for 10 min at room temperature (RT). Primary and secondary antibodies
754 were diluted in 3% (w/v) bovine serum albumin (BSA; Fisher) in PBS++. Samples were
755 first incubated with the primary antibody (α HA-1:1,000; α SAG-1:10,000; α GAP45-
756 1:5,000; α GRA3-1:1500; IV58B6-1:50) at RT for 45 min, washed 3x with PBS++, and
757 then incubated with fluorescent secondary antibodies (1:2,000) and 4',6-diamidino-2-
758 phenylindole (DAPI; 300 nM) for 45 min. Secondary antibodies (Invitrogen) were
759 conjugated to either Oregon Green or Texas Red fluorophores and specific to the
760 species and class of primary antibody used. Samples were then washed 3x with PBS++
761 before mounting the coverslip on a glass slide using MOWIOL mounting media.
762 Immunofluorescence staining was visualized using a Zeiss AxioVision upright
763 microscope with a 100X 1.4 numerical-aperture oil immersion objective, and images

764 were acquired using a grayscale Zeiss AxioCam MRM digital camera. Grayscale
765 images were pseudo-colored in ImageJ using magenta (Texas Red), yellow (Oregon
766 Green), and cyan (DAPI), and further alterations to brightness and contrast were also
767 made in ImageJ when deemed appropriate. For all assays in which staining intensity
768 was compared across treatments and parasite lines, concentrations of antibodies,
769 exposure times, and alterations to brightness/contrast were identical. Colocalization of
770 fluorescent antibodies/reagents was quantified using Pearson's coefficient calculated
771 with the JACoP plugin on ImageJ (94).

772 ***PAS staining-tachyzoite and in vitro bradyzoite***

773 PAS staining of tachyzoites and in vitro bradyzoites was done on infected HFFs fixed in
774 4% PFA and permeabilized as above. Coverslips were then washed 3x in tap water
775 before the addition of 1% periodic acid (Sigma-Aldrich) for 5 min. Coverslips were then
776 washed with three changes of tap water. Schiff's reagent (diluted 1:4 in tap water) was
777 added for 15 min. Coverslips were subsequently washed 10x with tap water to develop
778 stain before being incubated with DAPI for 10 min and then mounted as above. PAS-
779 stained samples were visualized using fluorescence microscopy (excitation: 545 nm,
780 emission: 605 nm). When PAS was co-stained with antibodies, primary antibodies were
781 incubated with PAS-stained slides overnight in BSA at 4 °C before standard secondary
782 staining.

783 PAS labeling of methanol fixed tissue cysts was performed as described elsewhere,
784 using Schiff reagent diluted 1:10 in tap water as described elsewhere ().

785

786 Samples treated with acid- α -amylglucosidase (GAA) (from *Aspergillus niger*, >260
787 U/mL, Sigma) were incubated with GAA after permeabilization. GAA was diluted 1:50 in
788 50 mM sodium phthalate buffer, pH 5.5, and samples were treated for 24 h at room
789 temperature. Untreated controls were incubated in phthalate buffer without GAA.
790 Samples were then stained with PAS or IV58B6 as described in the IF-staining workflow
791 above.

792 ***In vitro* bradyzoite conversion assay**

793 Tachyzoites were converted to bradyzoites *in vitro* using alkaline stress as has been
794 done previously with several modifications (95). HFFs grown were infected with
795 tachyzoites in standard cell culture media. 4 h later, media was replaced with RPMI
796 1640 (Gibco 31800022) supplemented with 50 mM HEPES and adjusted to pH 8.2 with
797 NaOH. Parasites were then cultured for 2-6 days at 37°C, ambient CO₂, and sealed in
798 Parafilm. Media was replaced every other day to maintain the basic pH. Parasites were
799 fixed in PFA and stained with fluorescein conjugated *Dolichos biflorus* agglutinin (DBA;
800 1:1000, Vector Laboratories) and PAS. Images were obtained in grayscale on a Zeiss
801 AxioVision upright microscope as described above. To determine the degree of labeling
802 with DBA or PAS, the Fiji/ImageJ (96) was used to create a binary mask outlining cysts
803 that was applied to the PAS-stained image to measure the greyscale intensity of each
804 ROI (i.e. each individual vacuole/*in vitro* cyst).

805 ***Transmission electron microscopy of in vitro tachyzoites and bradyzoites***

806 Transmission-electron microscopy (TEM) was performed as done previously (97).
807 Blocks were stained at the University of Kentucky's Imaging Center in the College of
808 Arts and Sciences. Blocks were trimmed and sectioned on an ultramicrotome with a

809 diamond knife. Sections were placed on copper grids and then contrast stained with
810 lead citrate. Micrographs were collected at the University of Kentucky's Electron
811 Microscopy Center on a Talos F200X TEM (Thermo) operated at 200 kV accelerating
812 voltage with a 50 μm objective aperture inserted to enhance contrast using a 16M pixel
813 4k x 4k CMOS camera (Ceta, Thermo Scientific). AG size and grayscale values were
814 measured in ImageJ.

815 ***Immunoblotting***

816 Parasites were syringe lysed from host cells, pelleted, and 2×10^6 parasites were
817 resuspended in SDS-PAGE sample buffer and boiled for 10 min before being run on a
818 single lane of a 10% polyacrylamide gel. The gel was then transferred to a 0.2 μm
819 PVDF membrane (BioRad) using a Turbotransfer System (BioRad) for 7 min at 25 V.
820 The PVDF membrane was blocked in 5% (w/v) non-fat milk in Tris-buffered saline plus
821 Tween-20 detergent (TBST; 0.1% Tween-20) for 20 min before being probed with a
822 primary antibody ($\alpha\text{HA-1:1,000}$; $\alpha\text{GAP45-1:5,000}$; $\alpha\text{SRS9-1:1,000}$; $\alpha\text{SAG1-1:10,000}$) in
823 non-fat milk overnight at 4°C (Cell Signaling C29F4). The blot was washed 3x with
824 TBST before probing with either HRP-conjugated α -rabbit or α -mouse-IgG (Jackson
825 Laboratories). Blot was washed and developed for 5 min using SuperSignal™ West
826 Pico PLUS (Thermo Scientific) and visualized on a GelDoc station (BioRad).

827 ***Steady state polar metabolite analysis***

828 Parasites were prepared as previously described (61). Confluent HFFs were infected
829 with parasites at a multiplicity of infection (MOI) of 2 to achieve a high density of
830 parasites after 48 h of growth (>80% cells containing >32 parasites each). Plates
831 containing infected HFFs were placed on ice, media removed, and the monolayer was

832 washed 2X with ice-cold PBS. Parasites were harvested on ice in a 4 °C cold-room.
833 Cells were scraped from plate surface, resuspended in PBS (8 plates/50 mL PBS), and
834 centrifuged at 1000g for 10 min at 4 °C. PBS was removed, the cell pellet was
835 resuspended in 2 mL PBS, and syringe passaged successively in 23 G and 27 G
836 needles. The soluble host cell lysate was removed by centrifugation (1000g). The pellet
837 was resuspended in 5 mL PBS and host-cell debris was removed by syringe-filtering the
838 suspension through a 3 µm filter (Whatman). Filtered parasites were then pelleted,
839 resuspended in 1 mL PBS, and counted on a hemacytometer. Parasites were pelleted a
840 final time at 14,000g for 30 s at 4 °C, supernatant was removed, and pelleted parasites
841 were flash frozen in liquid nitrogen and stored at -80 °C until metabolite extraction.

842 *Polar metabolite extraction:* Polar metabolites were extracted in 0.5 mL -20 °C 50%
843 methanol (MeOH) containing 20 µM L-norvaline (procedural control) for 30 min on ice.
844 During the 30 min incubation, samples were regularly vortexed. Samples were then
845 centrifuged at 14000g for 10 min to pellet insoluble material (protein, DNA, RNA, and
846 glycans). Supernatant containing polar metabolites and pellet were dried separately on
847 a SpeedVac (Thermo) at 10⁻³ mBar until methanol (MeOH) was completely sublimated
848 and only dried pellet remained.

849 *Pellet hydrolysis and extraction:* Dried fraction containing protein was hydrolyzed by
850 resuspending the pellet in 2 N HCl (final concentration) at 95°C for 2 h. Hydrolysis was
851 quenched, and hydrolyzed amino acids were extracted by the addition of an equal
852 volume of 100% MeOH with 40 µM L-norvaline such that the final concentration was
853 50% and 20 µM, respectively. Extraction and drying then proceeded as described
854 above.

855 *Sample derivatization:* Dried samples (both polar metabolites and hydrolyzed protein)
856 were derivatized in 70 μ L 20 mg/mL methoxyamine hydrochloride in pyridine for 90 min
857 at 30 °C. Samples were then centrifuged at 14000g for 10 min to remove any
858 particulate, and 50 μ L of the methoxyamine supernatant was mixed with 80 μ L *N*-
859 methyl-*N*-trimethylsilyl trifluoroacetamide (MSTFA) and incubated for 30 min at 37°C.
860 Samples were then transferred to amber glass chromatography vials and analyzed by
861 GC/MS.

862 *GC/MS analysis:* Metabolites were analyzed on an Agilent 7800B GC coupled to a
863 5977B MS detector using a previously established protocol (98). Automated Mass
864 Spectral Deconvolution and Identification System (AMDIS) was used to analyze
865 metabolites by matching metabolites to the FiehnLib metabolomics library via retention
866 time and fragmentation pattern. Quantification of metabolite levels was performed in
867 Mnova. Sample abundance was normalized to L-norvaline (procedural control) and
868 protein from the protein pellet (experimental control). Steady state metabolites are
869 presented as the mean of three independent replicates.

870

871

872 ***Conventional plaque assays***

873 HFFs were grown in 12-well plates until confluent. HFFs were subsequently infected
874 with 200 parasites/well under standard cell culture conditions. Wells were washed with
875 PBS to remove residual invasion media, and media was changed to glutamine replete
876 or depleted media 4 h post-infection to allow for invasion. Plates remained undisturbed
877 for 10 days before the infected HFFs were fixed with 100%, -20°C MeOH for 20 min,

878 stained with 1% crystal violet solution for 20 min, and then the plaques were de-stained
879 with repeated tap water washes. Zones of lysis (white clearings) could be visualized
880 against intact cells (purple). Images of plaques were obtained by scanning plates on an
881 Epson Perfection V600 photo scanner at a resolution of 600 dpi. The plaques were
882 measured by pixel area using ImageJ. Plaque assays were conducted on three
883 independent replicates, and plaque size from these experiments were aggregated to
884 highlight variability in plaque sizes.

885 ***Modified plaque assays***

886 A modified plaque assay was developed to visualize foci of infection at higher
887 magnification where zones of clearing were not readily evident. Confluent HFF
888 monolayers on glass coverslips in 24 well plates were infected with WT, Δ TgLaf, and
889 COMP parasites in replete media for 4 hours to allow for invasion. The monolayers
890 were washed gently 3 times with PBS and either fresh replete media or glutamine-
891 depleted media were added for 3 or 6 days to appropriate wells. Infected monolayers
892 were washed and fixed with MeOH (-20 °C) and subjected to IF using DAPI and GRA3,
893 an antibody that detects the PVM. Individual plaques were imaged on coded blinded
894 slides using a 10X objective, and their perimeters and encompassed areas were
895 measured using Image J. Host cell clearance within plaques was similarly measured,
896 and the extent of clearance was represented as a percentage for each individual
897 plaque. A total of three independent replicates were performed.

898 ***Egress assays***

899 HFFs were grown to confluency in 35 mm glass bottom dishes (MatTek, P35G-0-14-C).
900 Two days before infecting HFFs on glass bottom dishes, both HFFs and parasites were

901 independently pre-treated in either glutamine-replete or -depleted media (see above for
902 media formulations). After 48 h pre-treatment, 10^5 parasites of each line (WT, Δ TgLaf,
903 and COMP) in each pre-treatment (gln+/-) were added to fresh dishes and allowed to
904 grow for 48 h so that most vacuoles contained >32 parasites each. Several hours before
905 egress, media in each infected plate was adjusted to 1.5 mL and allowed to equilibrate
906 at 37°C in 5% CO₂. The calcium ionophore A23187 (Cayman Chemical Company) was
907 prepared as a 2 mM stock in DMSO and diluted in (+/-) gln media to make a 4X
908 concentration of 12 μ M and maintained at 37°C throughout the assay. Zaprinst was
909 likewise prepared as a 100 mM stock in DMSO and diluted into media at a 4X
910 concentration of 2 mM. Egress was triggered by the addition of 0.5 mL 4X A23187 to
911 infected HFFs (3.0 μ M final concentration) or 0.5 mL 4X-zaprinst (500 μ M final
912 concentration). Egress was monitored on a Nikon Eclipse Ti2 inverted microscope with
913 a 40X phase air objective modified with a 1.5X optivar. Several fields containing
914 vacuoles were selected from each plate, and an image was obtained 10 s after
915 triggering egress from each field once every 5 s for 5 mins (61 images/field) on a Nikon
916 DS-Ri2 color camera. Videos of each field were assembled on NIS Elements software.
917 Egress was monitored using standard deviation of pixel intensity and determined by
918 inflection point of change in standard deviation of pixel intensity. Inflection point was
919 calculated by fitting a gaussian curve to the first derivative of the standard deviation in
920 pixel intensity and calculating the mean of the curve. Technical replicates (fields on
921 each plate) were averaged for each biological replicate (average of fields from each
922 plate).

923 ***Replication assays***

924 HFFs were grown on glass coverslips in a 24-well plate until confluent. Two days before
925 infecting HFFs on coverslips, both HFFs and parasites were independently pre-treated
926 in either glutamine-replete or -depleted media. After pre-treatment, 10^4 parasites of
927 each line (WT, Δ TgLaf, and COMP) in each condition (gln+/-) were added to 3
928 coverslips each. 24 hours later, infected HFFs were fixed in MeOH and stained with Rb-
929 α -SAG1 (1:10,000) and DAPI for ease of visualization. Counting of parasites/vacuole
930 was performed for each line/condition on coded blinded slides with the identity of
931 samples revealed upon completion of the counting. A total of three independent
932 replicates were performed.

933

934 ***Mouse infection studies***

935 4- to 6-week old CBA/J mice of both sexes (Jackson Laboratories, Bar Harbor, ME)
936 were injected intraperitoneally (i.p.) with either 100 WT, Δ TgLaf, or COMP tachyzoites,
937 or with 20 tissue-cysts from brain homogenates derived from previously infected mice.
938 In either case, parasites/cysts were suspended in a final volume of 0.2 mL serum-free,
939 Opti-MEM media (Gibco). Mice were then monitored and assigned a body index score
940 daily. Monitoring frequency increased to twice a day once symptomatic throughout the
941 course of infection as previously described (52). When symptomatic, mice were
942 administered a gel diet and wet chow on the cage floor and given 0.25-0.5 mL saline
943 solution subcutaneously as needed. Moribund mice were humanely euthanized.
944 Euthanasia of both moribund mice and mice sacrificed at the time of tissue cyst harvest
945 was performed by CO₂ asphyxiation, followed by cervical dislocation. The number of
946 mice used for each experiment is indicated within relevant figures. All protocols were

947 carried out under the approval of the University of Kentucky's Institutional Animal Care
948 and Use Committee (IACUC).

949 ***Tissue cyst purification***

950 Tissue cysts were purified as previously described using discontinuous Percoll
951 gradients (11, 70). Processing of two sex/infection-matched brains was performed on
952 each gradient. Cysts were collected in 1 mL fractions from the bottom of the centrifuged
953 Percoll gradient using a peristaltic pump adjusted to a flow rate of 2 mL/min. To quantify
954 tissue cysts, 10-20 μ L of each fraction was placed into 100 μ L PBS in the well of a 96-
955 well plate, pelleted and directly enumerated at 20X magnification in each well. Total
956 cysts per mouse were calculated by summing the total number of cysts in each fraction
957 and dividing the total by two to adjust for brain homogenization in pairs. Each pair of
958 mice was presented as a single averaged data point. Tissue cysts were pelleted onto
959 slides using a Cytospin centrifuge and fixed and stored in 100% MeOH (-20°C) until
960 staining.

961 ***Quantification of AG levels in tissue cysts based on PAS labeling intensity.***

962 Tissue cysts deposited on glass slides were fixed and stored in methanol at -20°C.
963 Slides were equilibrated to room temperature and stained with PAS using conditions
964 optimized for staining tissue cysts (14). Cysts were additionally stained with DBA lectin
965 to demarcate the cyst boundary. Thirty randomly acquired cysts were imaged using a
966 fixed exposure as a z-stack with a 0.24 μ m step, with the center slice used for
967 quantification without deconvolution using AmyloQuant, a purpose developed
968 quantitative imaging based application (14). The distribution of pixel intensities was
969 defined in 4 bins representing the background (black: 0-10 grayscale), low (blue: 10-25),

970 intermediate (green: 25-50) and high (red: >50) proportion of pixels (14). The relative
971 distribution of PAS intensities across the 4 bins is represented using a stacked plot with
972 the distribution patterns arrayed from lowest to highest intensity for each cohort.
973 AmyloQuant additionally presents a spatial heat map to allow for the distribution of PAS
974 intensity (AG) to be revealed within the imaged cyst. The mean pixel intensity of each
975 cyst was additionally determined following the definition of the ROI defined by the
976 boundary of the cyst wall using Image J. Measurements of cyst diameters in microns
977 was achieved using the Zeiss Zen imaging software.

978 ***Preparation of in vivo tissue cysts for TEM imaging***

979 To prepare *T. gondii* tissue cysts generated *in vivo* for TEM, cysts were isolated from
980 the brains of infected mice as detailed above through the counting step. The Percoll
981 fraction containing mouse red blood cells (RBCs) was also recovered. After combining
982 Percoll fractions containing tissue cysts and diluting with PBS to a volume of 15 mL
983 (maximum of two 1-mL fractions were combined before dilution), cysts were pelleted for
984 15 min at 1000g at 4 °C. To maximize cyst recovery, 10 mL supernatant was removed,
985 and the remaining 5 mL was divided into 1 mL fractions for the top 4 mL, and the bottom
986 1 mL directly above the pellet was sub-fractionated into 100 µL volumes. Typically, the
987 majority of cysts were localized to within 300 µL of the Percoll pellet, rather than in the
988 pellet itself. Sub-fractions containing cysts were once again combined and diluted
989 (typically 200-300 µL diluted with 1-mL PBS) in a 1.5 mL Eppendorf tube, and then
990 pelleted in a swinging-bucket rotor for 10 min at 1000g and 4 °C. Leaving the pellet
991 undisturbed, all but 50 µL of the supernatant was removed. A small volume (~5-10 µL)

992 of the reserved RBC fraction was added to the remaining volume for ease of visualizing
993 the pellet throughout the remaining processing steps.

994 To ensure the detection of the relatively rare cyst population, a previously described
995 protocol (71, 72) was adapted to concentrate the cysts into a small agarose block. A
996 1.33X fixative solution of glutaraldehyde (GA) in cacodylate buffer was prepared
997 containing 4% GA and 133 mM sodium cacodylate. 150 μ L fixative solution was then
998 added to the 50 μ L sample, bringing the total volume to 200 μ L such that the final
999 concentration of GA was 3% and sodium cacodylate was 100 mM. Cysts were then
1000 incubated at room temperature for 1 h in fixative. While cysts were in fixative, 4% low-
1001 melt agarose (BioRad) was prepared in 100 mM sodium cacodylate buffer and kept
1002 liquid at 70 °C until needed. After fixation, cysts were pelleted again at 1000g for 10 min
1003 at room temperature in a table-top centrifuge. All but 50 μ L supernatant was once again
1004 removed, and 200 μ L warm low-melt agarose was slowly added on top of fixed, pelleted
1005 cysts (3.2% agarose, final concentration). Suspension was then centrifuged again at
1006 1000g for 10 min at 30 °C to keep the agarose semi-liquid, and then placed on ice for
1007 20 min to solidify agarose. After solidification, entire agarose plug was removed from
1008 tube with a small a wooden dowel that had been whittled into a thin scoop. This agarose
1009 plug was placed in a Petri dish, and the pellet was carefully cut out of the plug with a
1010 razor blade to create a 1 mm³ block. The agarose block was then stored in 1X
1011 GA/cacodylate buffer overnight at 4°C. Processing of the block from post-stain onward
1012 was then identical to TEM processing described above. During sectioning, thick
1013 sections cut on a glass knife were stained with toluidine blue and examined for cysts

1014 using a light microscope prior to ultra-thin sectioning once the cyst containing later was
1015 identified.

1016 **Data analyses**

1017 All data analyses, including graph preparation and statistics, were performed using
1018 GraphPad Prism 9 or 10. Details on statistical tests applied are presented in the specific
1019 figure legends.

1020

1021 **Figure Legends.**

1022 **Figure 1.** Glucan dynamics in *T. gondii* ME49 tachyzoites and in vitro bradyzoites.

1023 **A,** Microscopy-based glucan evaluation of *T. gondii* tachyzoites and bradyzoites using
1024 PAS (left), IV58B6 (middle; α -glycogen IgM mAb), and TEM (right). **B,** GAA digest of
1025 AGs in tachyzoites and bradyzoites confirms specificity of IV58B6 antibody and PAS
1026 staining. All scale bars = 5 μ m.

1027

1028 **Figure 2.** Endogenous epitope tagging and localization of TgLaforin.

1029 **A,** Schematic depicting the TgLaforin 3xHA-epitope tagging strategy. X = stop codon. **B,**
1030 Successful tagging of TgLaforin (62 kDa) was verified using immunoblot analysis with
1031 an α -HA antibody with SAG1 used as a loading control. **C,** IFA of Wild type (WT) and
1032 TgLaforin-3XHA (TgLaf-HA) tagged parasites with α -HA antibody under tachyzoite and
1033 in vitro bradyzoite conditions. Stage conversion is confirmed by Dolichos lectin (DBA)
1034 staining. **D,** Western blot analysis of TgLaforin expression levels in tachyzoites (T) and
1035 in vitro bradyzoites (B). Expression of TgLaf-HA is absent under in vitro bradyzoite
1036 conditions. GAP45 is the loading control. Decrease in SAG1 alongside increase in

1037 SRS9 confirms tachyzoite to bradyzoite conversion. **E**, IFA of TgLaforin-HA
1038 colocalization with PAS. Pearson's coefficient: 0.765. **F**, IFA of TgLaforin-HA
1039 colocalization with IV58B6. Pearson's coefficient: 0.737. All scale bars = 5 μ m.

1040

1041 **Figure 3.** Loss of TgLaforin results in no gross glucan abnormalities under glucose
1042 replete conditions. **A**, Schematic of TgLaforin KO strategy: the pyrimethamine-
1043 resistance DHFR* gene containing 40-nt homologous arms (dark gray boxes on either
1044 end of gene) was inserted into the TgLaforin locus via homologous recombination. A
1045 double stranded break was induced using CRISPR/Cas9-GFP with a PAM site in the
1046 first exon. **B**, Inside/out PCR verification of DHFR integration into the TgLaforin locus.
1047 Amplicons (PCR1-4) are illustrated in (A). **C**, Loss of TgLaforin mRNA was confirmed by
1048 amplifying full-length TgLaforin cDNA generated from both WT and Δ TgLaf strains.
1049 Actin cDNA amplification serves both as a loading control and as a control to verify the
1050 absence of gDNA. **D**, Analysis of glucan levels in Δ TgLaf tachyzoites using three
1051 different approaches: PAS and IV58B6 immunofluorescence staining, and TEM.

1052

1053 **Figure 4.** Δ TgLaf parasites are dependent on glutamine for normal plaque formation.
1054 **A**, Steady-state metabolomics suggests upregulation of glutaminolysis in Δ TgLaf
1055 parasites. Metabolite levels of intracellular tachyzoites were analyzed after 48 hours of
1056 growth in HFFs by GC/MS analysis. Data were collected from 3 independent replicates.
1057 Statistical comparisons were done using unpaired two-tailed t-tests. Statistical
1058 significance is as follows: ** $p < 0.01$, ns= $p > 0.05$, nd=not detected.

1059 **B**, Representative plaque assays following staining of infected HFF monolayers with
1060 crystal violet under nutrient replete (+gln) and glutamine free (gln-) conditions. WT,
1061 Δ TgLaf (KO) and complemented (COMP) lines were evaluated.

1062 **C**, Quantification of visible plaques for WT, Δ TgLaf and COMP lines under nutrient
1063 replete and glutamine free conditions represented as the plaque area (pixels) was
1064 measured across three independent replicates 6 days following infection.

1065 **D**, Pixel area of nascent plaques/vacuoles after 3 days of growth as monitored by IFA
1066 microscopy following staining with the PVM marker GRA3 under both glutamine replete
1067 (+) and depleted conditions (-). **E**, Pixel area of plaques monitored as in (D) after 6 days
1068 of growth. Statistical comparisons for C-E were done using an ordinary one-way
1069 ANOVA using Tukey's post-hoc test to correct for multiple comparisons. Statistical
1070 significance is indicated as follows: * $p < 0.05$, **** $p < 0.0001$, ns= $p > 0.05$.

1071

1072 **Figure 5.** Loss of TgLaforin results in aberrant glucan morphology and accumulation in
1073 *in vitro* bradyzoites only visible by TEM. **A**, *In vitro* tachyzoite to bradyzoite conversion
1074 efficiency of Δ TgLaf vs WT parasites as measured by DBA intensity confirms no defect
1075 in induced stage conversion in Δ TgLaf parasites. **B**, Change in AG levels detected
1076 using the intensity of PAS labeling during bradyzoite conversion reveals no statistically
1077 different levels in AG accumulation based on PAS intensity. **C**, Representative TEM
1078 images of bradyzoites from each indicated parasite line. At 4300x magnification, scale
1079 bar = 2 μ m; at 8600x magnification, scale bar = 1 μ m. Arrowhead = canonical AG
1080 (white, round/ovoid); Arrow = aberrant AG (grey, flattened, multi-lobed). **D**,
1081 Quantification of relative parasite AG content and **E**, AG grayness across parasite lines

1082 using 8-bit grayscale (0=black, 255=white). Statistical comparisons were done using an
1083 ordinary one-way ANOVA with Tukey's post-hoc test to correct for multiple
1084 comparisons. Statistical significance is indicated as follows: * $p < 0.05$, *** $p < 0.001$,
1085 **** $p < 0.0001$, ns= $p > 0.05$.

1086

1087 **Figure 6.** Loss of TgLaforin attenuates tachyzoite virulence and cyst burden in mice.
1088 Equal numbers of male and female CBA/J mice were infected i.p. with 100 tachyzoites
1089 from each group and monitored for both symptom progression and mortality.

1090 **A**, Symptomology throughout the acute (< day 20) and early chronic phases of infection
1091 (day 21-28). Mice were monitored 1-2x/day and assigned a body score index ranging
1092 from asymptomatic (Stage 0) to moribund/deceased. Staging of disease progression is
1093 discussed in (52). **B**, Kaplan-Meier curve of mouse survival throughout acute and early
1094 chronic infection following tachyzoite infection. **C**, A cohort of mice that survived 4-
1095 weeks were euthanized, and the cyst burden determined as done previously described
1096 (70). Error bars depict SD from the mean. Statistical comparison for Kaplan Meier
1097 curves is indicated on plot, and statistical comparison of cyst burden was done using
1098 unpaired two-tailed t-tests. Statistical significance: * $p < 0.05$, *** $p < 0.0002$.

1099

1100 **Figure 7.** Mouse infection with Δ TgLaf tissue cysts results in milder illness and lower
1101 cyst burden. CBA/J mice were infected i.p. with 20 cysts taken from previously infected
1102 mouse brains and monitored for symptomology and death. Tissue cysts were harvested
1103 from mice infected for 4 or 6 weeks respectively. **A**, Symptomology throughout the
1104 acute and early chronic phase of infection as described in Figure 6B. **B**, Kaplan-Meier

1105 curve of mouse survival during the acute and early chronic infection reveal low overall
1106 mortality associated with cyst initiated infections for all parasite lines. **C**, Tissue cyst
1107 burden following a 4-week bradyzoite initiated infection. Cyst numbers were determined
1108 as described in Figure 6C. Statistical comparison of cyst burden was done using
1109 unpaired two-tailed t-tests. Statistical significance: * $p < 0.05$, ns= $p > 0.05$.

1110

1111 **Figure 8.** Quantification of amylopectin levels in tissue cysts based on PAS intensity.

1112 **A.** The mean intensity of PAS labeled tissue cysts measured using Image J for WT,
1113 Δ TgLaf and COMP tissue cysts harvested at 4 and 6 weeks post infection reveal no
1114 difference in AG levels across these parasite lines at week 4. Highly significant
1115 differences are evident between WT/COMP and DTgLaf tissue cysts at week 6 post
1116 infection indicating a temporal component for the emergence of the starch excess
1117 phenotype. $n=30$ for each parasite line at each time point of harvest. Statistical analysis
1118 was done using Tukey's multiple comparison test. P values: * $p < 0.05$, **** $p < 0.0001$

1119 **B.** Analysis of WT, DTgLaf and COMP tissue cysts harvested at weeks 4 and 6 using
1120 AmyloQuant. The 30 tissue cysts per sample presented in A. were analyzed using
1121 AmyloQuant. While acquired at random, the data are arrayed from low to high PAS
1122 intensity presented as the percentage of pixels in each classification bin. The
1123 classification bins defined as: background: Black: 0-10 grayscale, low: Blue: 10-25
1124 grayscale, intermediate: Green 25-50 grayscale and high intensity pixels: Red >50
1125 grayscale. The higher overall sensitivity of AmyloQuant reveals increased accumulation
1126 of AG at week 4 in the DTgLaf and COMP lines. This phenotype is greatly exaggerated
1127 at week 6 post infection consistent with a temporal component for the phenotypic

1128 manifestation of the starch excess phenotype. The pattern in the COMP parasites is
1129 intermediate between the WT and Δ TgLaf cysts. The distribution of PAS intensity levels
1130 within the imaged tissue cysts generated by AmyloQuant for cysts in 5 cyst intervals is
1131 presented under each set of stacked plots.

1132

1133 **Figure 9.** Transmission electron microscopy of purified tissue cyst from infected mouse
1134 brains confirms the presence of aberrant AG accumulation within Δ TgLaf cysts. The
1135 accumulation of amylopectin granules within the cytoplasm of WT bradyzoites with
1136 parasites exhibiting different levels. Additionally, evidence of active endodyogeny is
1137 present. Δ TgLaf tissue cysts contain a mix of bradyzoites with expected cytoplasmic
1138 and organellar contrast as well as others with grossly exaggerated AG levels that and
1139 the apparent loss of both the cytoplasmic and organellar contents. The COMP line
1140 exhibits AG accumulation levels similar to that observed in WT parasites with the tissue
1141 cyst itself appearing to be very tightly packed, with high levels of granular material
1142 between individual bradyzoites. Upper panels: scale bar = 5 μ m; lower panels (zoom of
1143 boxed region from upper panel): scale bar = 2 μ m.

1144

1145 **Supplemental Files**

1146 **Supplemental File 1.**

1147 **Figure S1.** Schematic of TgLafarin complementation strategy and confirmation of
1148 successful expression of TgLafarin. **A.** Schematic of TgLafarin complementation into
1149 Δ TgLaf parasites in which a PAM site was chosen at a neutral locus previously
1150 identified in chromosome VI (99) to insert TgLafarin cDNA under its endogenous

1151 promoter. The TgLaforin construct was connected to the HXGPRT selectable drug
1152 marker and inserted using NHEJ. **B.** PCR confirmation of integration of TgLaforin
1153 construct into chromosome VI. Primer sets are indicated above amplicons. WT primers
1154 amplify the same locus as in Figure 3 (“PCR 1”), also present in the COMP line. KO
1155 primers amplify the chimeric locus depicted in Figure 3 (“PCR 2”). Presence of the KO
1156 amplicon confirms that KO locus remains intact in COMP line. COMP primers amplify
1157 the chimeric locus generated upon insertion of the complementation construct. VI
1158 primers amplify the native chromosome VI locus, which is lost only in the COMP line. **C,**
1159 Western blot confirms expression of TgLaforin-HA in complemented parasites. Tagged
1160 LAF-HA parasites serve as a comparison to confirm the correct MW (62 kDa) and
1161 expression level. **D,** IFA demonstrates restoration of cytoplasmic, punctate localization
1162 of TgLaforin. Scale bar = 5 μ m.

1163

1164 **Supplemental File 2**

1165 **Figure S2.** Loss of TgLaforin results in cumulative defects that cannot be pinpointed to
1166 a single aspect of lytic cycle. **A.** Calcium ionophore-stimulated egress assay in which
1167 parasites were pre-starved of glutamine for 48 hours, seeded onto HFFs and allowed to
1168 grow for 48 hours to produce vacuoles containing >16 parasites, and stimulated with 3
1169 μ M A23187. Egress was monitored by video microscopy, and time to egress was
1170 monitored as described in Materials and Methods. Data is the average of 3 biological
1171 replicates that each consist of 4-5 technical replicates. COMP experiments measured 2
1172 biological replicates. **B.** Zaprinast stimulated egress assay performed as described for
1173 ionophore, however 500- μ M zaprinast was used to stimulate egress. Data is the

1174 average of 3 biological replicates that each consist of 2-5 technical replicates. COMP
1175 experiments measured 2 biological replicates. **C.** Replication assay in which parasites
1176 were pre-starved of glutamine for 48 hours, re-seeded into HFFs, and counted after 24
1177 hours of growth. Numbers (2, 4, or 8) indicate the number of tachyzoites counted per
1178 vacuole. Data is the average of 3 biological replicates with at least 70 vacuoles counted
1179 per replicate. **D.** Representative images of plaque formation at days 3 and 6, +/-
1180 glutamine. Images were taken at 10X magnification using a SAG1 antibody to visualize
1181 vacuoles and developing plaque size. The boundaries of vacuoles/ plaques were traced
1182 manually to define their area. Regions of cell clearance was additionally scored. **E,**
1183 Percent of plaques cleared was measured at both days 3 and 6 by dividing the area of
1184 the clearing by total plaque size. Statistical comparisons were done using an ordinary
1185 one-way ANOVA using Tukey's post-hoc test to correct for multiple comparisons. Error
1186 bars depict SD from the mean. Statistical significance is indicated as follows:
1187 ns= $p>0.05$.

1188

1189 **Supplemental File 3**

1190 **Figure S3.** The loss of TgLaforin does not have any impact on distribution of tissue
1191 cyst sizes. **A.** Tissue cyst diameters of 30 cysts each per line (WT, Δ TgLaf, COMP) per
1192 time point (Week 4 and Week 6) were measured using DBA labeled cyst wall as the
1193 delimiter using the Zeiss Zen software functionality. While all lines exhibit considerable
1194 variability, no statistically significant differences in cyst size were noted in the DTgLaf
1195 mutant relative to WT and COMP cysts. **B.** The relationship between tissue cyst size

1196 and AG accumulation defined by mean PAS intensity was not found to have any
1197 significant correlation.

1198

1199 **Supplemental File 4**

1200 **Figure S4.** Additional images of *in vivo* tissue cysts. **A.** A WT tissue cyst with two
1201 zoomed in areas (orange and yellow dashed line boxes) exhibit variability in the levels
1202 of AG and present with well defined cytoplasmic and organellar contents. **B.** A Δ TgLaf
1203 tissue cyst presents with a mix of bradyzoites with both cytoplasmic and organelles as
1204 well as bradyzoites lacking clearly defined organelles and/or cytoplasm. In addition
1205 enucleated bradyzoites are evident (asterisks) as well as the displacement of rhoptries
1206 by elevated levels of AG in the cytoplasm. Left column scale bar = 5 μ m; right column
1207 zoom scale bars = 2 μ m.

1208

1209 **Supplemental File 5**

1210 **Supplemental Table 1.** sgRNA sequences used in this study.

1211

1212 **Supplemental File 6**

1213 **Supplemental Table 2.** Plasmid constructs used in this study.

1214

1215 **Supplemental File 7**

1216 **Supplemental Table 3.** DNA primer sequences and their application in this study

1217 -----

1218 **Acknowledgements:** The authors wish to acknowledge Dr. Elizabeth Watts who
1219 conducted early exploratory studies that encouraged the pursuit of this project, Jim
1220 Begley (Imaging Center, University of Kentucky) for preparation of EM samples and
1221 willingness to explore new methodologies for isolating rare *in vivo* cysts, Jillian Cramer
1222 (Electron Microscopy Center, University of Kentucky) for acquisition of TEM images,
1223 and Jennifer Strange (Flow Cytometry and Immune Monitoring Core Facility, University
1224 of Kentucky) for assistance with isolation of GFP+ *T. gondii* mutants using flow
1225 cytometry.

1226 We additionally thank Dr's David Sibley (Washington University) and Peter Bradley
1227 (UCLA) for their gifts of DNA constructs and antibodies.

1228

1229 **Author contributions:**

1230 Conceptualization (R.D.M., A.P.S., M.S.G.), Methodology (R.D.M., A.D., C.O.B., A.T.,
1231 A.P.S., M.S.G.), Formal analysis (R.D.M., C.A.T., J.S.M., L.E.A.Y., R.C.S., A.T, A.P.,
1232 C.W.V.K., A.P.S.), Investigation (R.D.M., C.A.T., J.S.M., L.E.A.Y., A.P.S.), Resources
1233 (M.S.G., A.P.S.), Writing—original draft (R.D.M., A.P.S.), Writing—review and editing
1234 (all authors), Visualization (R.D.M., C.A.T., J.S.M., A.P.S.), Supervision (M.S.G.,
1235 A.P.S.), Project administration (R.D.M., M.S.G., A.P.S.), Funding acquisition (R.D.M.,
1236 C.W.V.K., M.S.G., A.P.S.).

1237

1238 **Funding:** This work was supported by: GRFP 1247392 to R.D.M., NIH grants R21
1239 AI150631 to A.P.S and R01 AI145335 to A.P.S. and A.P, and NIH grants R35

1240 NS116824, P01 NS097197, and NSF CHE 1808304 to C.W.V.K. and MCB 2308488 to
1241 M.S.G.

1242

1243 **Conflicts of Interest:** none

1244

1245 **Abbreviations:** AG, amylopectin granule; CDPK2, calcium dependent protein kinase2;
1246 COMP, TgLaforin-complemented parasite line; CRISPR, clustered regularly
1247 interspersed short palindromic repeats; DBA, *Dolichos biflorus* agglutinin lectin; Δ TgLaf,
1248 TgLaforin-KO parasite line; DHFR, dihydrofolate reductase; FACS, fluorescence
1249 activated cell sorting; GAA, acid- α -amylglucosidase; Gal-NAc, N-acetylgalactosamine;
1250 GAPDH1, glyceraldehyde-3-phosphate dehydrogenase; GC/MS, gas
1251 chromatography/mass spectrometry; GFP, green fluorescent protein; GT1, glucose
1252 transporter1; GWD, glucan, water di-kinase; HA, hemagglutinin; HFF, human foreskin
1253 fibroblasts; HK, hexokinase; HR, homologous recombination; HXGPRT, hypoxanthine-
1254 xanthine-guanine phosphoribosyl transferase; IF, immunofluorescence; i.p.,
1255 intraperitoneally; KO, knockout; MPA, mycophenolic acid; PAM, protospacer adjacent
1256 motif; PAS, periodic acid-Schiff; PV, parasitophorous vacuole; PWD, phospho-glucan,
1257 water di-kinase; PYK1, pyruvate kinase1; RBC, red blood cell; RT, room temperature;
1258 SEX4, starch-excess4; SS, starch/glycogen synthase; TCA, tricarboxylic acid; TEM,
1259 transmission electron microscopy; UTR, untranslated region; WT, parental
1260 ME49 Δ HXGPRT parasite line used in this study.

1261

1262 **Literature Cited**

- 1263 1. Flegr J, Prandota J, Sovickova M, Israili ZH. 2014. Toxoplasmosis--a global threat.
1264 Correlation of latent toxoplasmosis with specific disease burden in a set of 88
1265 countries. PLoS One 9:e90203.
- 1266 2. Tenter AM, Heckeroth AR, Weiss LM. 2000. *Toxoplasma gondii*: from animals to
1267 humans. Int J Parasitol 30:1217-58.
- 1268 3. Jones JL, Dubey JP. 2012. Foodborne toxoplasmosis. Clin Infect Dis 55:845-51.
- 1269 4. Derouin F, Garin YJ. 1991. *Toxoplasma gondii*: blood and tissue kinetics during
1270 acute and chronic infections in mice. Exp Parasitol 73:460-8.
- 1271 5. Pittman KJ, Knoll LJ. 2015. Long-Term Relationships: the Complicated Interplay
1272 between the Host and the Developmental Stages of *Toxoplasma gondii* during
1273 Acute and Chronic Infections. Microbiol Mol Biol Rev 79:387-401.
- 1274 6. Zhao XY, Ewald SE. 2020. The molecular biology and immune control of chronic
1275 *Toxoplasma gondii* infection. J Clin Invest 130:3370-3380.
- 1276 7. Luft BJ, Hafner R, Korzun AH, Leport C, Antoniskis D, Bosler EM, Bourland DD, 3rd,
1277 Uttamchandani R, Fuhrer J, Jacobson J, et al. 1993. Toxoplasmic encephalitis in
1278 patients with the acquired immunodeficiency syndrome. Members of the ACTG
1279 077p/ANRS 009 Study Team. N Engl J Med 329:995-1000.
- 1280 8. Luft BJ, Remington JS. 1992. Toxoplasmic encephalitis in AIDS. Clin Infect Dis
1281 15:211-22.
- 1282 9. Cerutti A, Blanchard N, Besteiro S. 2020. The Bradyzoite: A Key Developmental
1283 Stage for the Persistence and Pathogenesis of Toxoplasmosis. Pathogens 9.

- 1284 10. Sinai AP, Watts EA, Dhara A, Murphy RD, Gentry MS, Patwardhan A. 2016.
1285 Reexamining Chronic *Toxoplasma gondii* Infection: Surprising Activity for a
1286 "Dormant" Parasite. *Curr Clin Microbiol Rep* 3:175-185.
- 1287 11. Watts E, Zhao Y, Dhara A, Eller B, Patwardhan A, Sinai AP. 2015. Novel
1288 Approaches Reveal that *Toxoplasma gondii* Bradyzoites within Tissue Cysts Are
1289 Dynamic and Replicating Entities In Vivo. *MBio* 6:e01155-15.
- 1290 12. Place BC, Troublefield C, Murphy RD, Sinai AP, Patwardhan A. 2021. Computer
1291 Aided Image Processing to Facilitate Determination of Congruence in Manual
1292 Classification of Mitochondrial Morphologies in *Toxoplasma gondii* Tissue Cysts.
1293 *Annu Int Conf IEEE Eng Med Biol Soc* 2021:3509-3513.
- 1294 13. Place BC, Troublefield CA, Murphy RD, Sinai AP, Patwardhan AR. 2023. Machine
1295 learning based classification of mitochondrial morphologies from fluorescence
1296 microscopy images of *Toxoplasma gondii* cysts. *PLoS One* 18:e0280746.
- 1297 14. Tripathi A, Donkin RW, Miracle JS, Murphy RD, Patwardhan A, Sinai AP. 2024.
1298 Dynamics of amylopectin granule accumulation during the course of the chronic
1299 *Toxoplasma* infection is linked to intra-cyst bradyzoite replication. *bioRxiv*
1300 doi:10.1101/2024.09.02.610794:2024.09.02.610794.
- 1301 15. MacNeill GJ, Mehrpouyan S, Minow MAA, Patterson JA, Tetlow IJ, Emes MJ. 2017.
1302 Starch as a source, starch as a sink: the bifunctional role of starch in carbon
1303 allocation. *J Exp Bot* 68:4433-4453.
- 1304 16. Dubey JP, Lindsay DS, Speer CA. 1998. Structures of *Toxoplasma gondii*
1305 tachyzoites, bradyzoites, and sporozoites and biology and development of tissue
1306 cysts. *Clin Microbiol Rev* 11:267-99.

- 1307 17. Coppin A, Dzierszinski F, Legrand S, Mortuaire M, Ferguson D, Tomavo S. 2003.
1308 Developmentally regulated biosynthesis of carbohydrate and storage
1309 polysaccharide during differentiation and tissue cyst formation in *Toxoplasma*
1310 *gondii*. *Biochimie* 85:353-61.
- 1311 18. Guerardel Y, Leleu D, Coppin A, Lienard L, Slomianny C, Strecker G, Ball S,
1312 Tomavo S. 2005. Amylopectin biogenesis and characterization in the protozoan
1313 parasite *Toxoplasma gondii*, the intracellular development of which is restricted in
1314 the HepG2 cell line. *Microbes Infect* 7:41-8.
- 1315 19. Coppin A, Varre JS, Lienard L, Dauvillee D, Guerardel Y, Soyer-Gobillard MO,
1316 Buleon A, Ball S, Tomavo S. 2005. Evolution of plant-like crystalline storage
1317 polysaccharide in the protozoan parasite *Toxoplasma gondii* argues for a red
1318 alga ancestry. *J Mol Evol* 60:257-67.
- 1319 20. Uboldi AD, McCoy JM, Blume M, Gerlic M, Ferguson DJ, Dagley LF, Beahan CT,
1320 Stapleton DI, Gooley PR, Bacic A, Masters SL, Webb AI, McConville MJ, Tonkin
1321 CJ. 2015. Regulation of Starch Stores by a Ca(2+)-Dependent Protein Kinase Is
1322 Essential for Viable Cyst Development in *Toxoplasma gondii*. *Cell Host Microbe*
1323 18:670-81.
- 1324 21. Yang J, He Z, Chen C, Zhao J, Fang R. 2022. Starch Branching Enzyme 1 Is
1325 Important for Amylopectin Synthesis and Cyst Reactivation in *Toxoplasma*
1326 *gondii*. *Microbiol Spectr* 10:e0189121.
- 1327 22. Yang J, Yang C, Qian J, Li F, Zhao J, Fang R. 2020. *Toxoplasma gondii* alpha-
1328 amylase deletion mutant is a promising vaccine against acute and chronic
1329 toxoplasmosis. *Microb Biotechnol* 13:2057-2069.

- 1330 23. Lyu C, Yang X, Yang J, Hou L, Zhou Y, Zhao J, Shen B. 2021. Role of amylopectin
1331 synthesis in *Toxoplasma gondii* and its implication in vaccine development
1332 against toxoplasmosis. *Open Biol* 11:200384.
- 1333 24. Blume M, Nitzsche R, Sternberg U, Gerlic M, Masters SL, Gupta N, McConville MJ.
1334 2015. A *Toxoplasma gondii* Gluconeogenic Enzyme Contributes to Robust
1335 Central Carbon Metabolism and Is Essential for Replication and Virulence. *Cell*
1336 *Host Microbe* 18:210-20.
- 1337 25. Ralton JE, Sernee MF, McConville MJ. 2021. Evolution and function of carbohydrate
1338 reserve biosynthesis in parasitic protists. *Trends Parasitol* 37:988-1001.
- 1339 26. Sernee MF, Ralton JE, Nero TL, Sobala LF, Kloehn J, Vieira-Lara MA, Cobbold SA,
1340 Stanton L, Pires DEV, Hanssen E, Males A, Ward T, Bastidas LM, van der Peet
1341 PL, Parker MW, Ascher DB, Williams SJ, Davies GJ, McConville MJ. 2019. A
1342 Family of Dual-Activity Glycosyltransferase-Phosphorylases Mediates Mannogen
1343 Turnover and Virulence in Leishmania Parasites. *Cell Host Microbe* 26:385-399
1344 e9.
- 1345 27. Chen P, Lyu CC, Wang YD, Pan M, Lin XY, Shen B. 2023. Key roles of amylopectin
1346 synthesis and degradation enzymes in the establishment and reactivation of
1347 chronic toxoplasmosis. *Animal Diseases* 3.
- 1348 28. Stitt M, Zeeman SC. 2012. Starch turnover: pathways, regulation and role in growth.
1349 *Curr Opin Plant Biol* 15:282-92.
- 1350 29. Kotting O, Kossmann J, Zeeman SC, Lloyd JR. 2010. Regulation of starch
1351 metabolism: the age of enlightenment? *Curr Opin Plant Biol* 13:321-9.

- 1352 30. Silver DM, Kotting O, Moorhead GB. 2014. Phosphoglucan phosphatase function
1353 sheds light on starch degradation. *Trends Plant Sci* 19:471-8.
- 1354 31. Ritte G, Lloyd JR, Eckermann N, Rottmann A, Kossmann J, Steup M. 2002. The
1355 starch-related R1 protein is an alpha -glucan, water dikinase. *Proc Natl Acad Sci*
1356 U S A 99:7166-71.
- 1357 32. Kotting O, Pusch K, Tiessen A, Geigenberger P, Steup M, Ritte G. 2005.
1358 Identification of a novel enzyme required for starch metabolism in Arabidopsis
1359 leaves. The phosphoglucan, water dikinase. *Plant Physiol* 137:242-52.
- 1360 33. Edner C, Li J, Albrecht T, Mahlow S, Hejazi M, Hussain H, Kaplan F, Guy C, Smith
1361 SM, Steup M, Ritte G. 2007. Glucan, water dikinase activity stimulates
1362 breakdown of starch granules by plastidial beta-amylases. *Plant Physiol* 145:17-
1363 28.
- 1364 34. Hejazi M, Fettke J, Haebel S, Edner C, Paris O, Froberg C, Steup M, Ritte G. 2008.
1365 Glucan, water dikinase phosphorylates crystalline maltodextrins and thereby
1366 initiates solubilization. *Plant J* 55:323-34.
- 1367 35. Hansen PI, Spraul M, Dvortsak P, Larsen FH, Blennow A, Motawia MS, Engelsen
1368 SB. 2009. Starch phosphorylation--maltosidic restrains upon 3'- and 6'-
1369 phosphorylation investigated by chemical synthesis, molecular dynamics and
1370 NMR spectroscopy. *Biopolymers* 91:179-93.
- 1371 36. Murphy RD, Chen T, Lin J, He R, Wu L, Pearson CR, Sharma S, Vander Kooi CD,
1372 Sinai AP, Zhang ZY, Vander Kooi CW, Gentry MS. 2022. The Toxoplasma
1373 glucan phosphatase TgLaforin utilizes a distinct functional mechanism that can
1374 be exploited by therapeutic inhibitors. *J Biol Chem* 298:102089.

- 1375 37. Kotting O, Santelia D, Edner C, Eicke S, Marthaler T, Gentry MS, Comparot-Moss S,
1376 Chen J, Smith AM, Steup M, Ritte G, Zeeman SC. 2009. STARCH-EXCESS4 Is
1377 a Laforin-Like Phosphoglucan Phosphatase Required for Starch Degradation in
1378 *Arabidopsis thaliana*. *Plant Cell* 21:334-46.
- 1379 38. Minassian BA, Lee JR, Herbrick JA, Huizenga J, Soder S, Mungall AJ, Dunham I,
1380 Gardner R, Fong CY, Carpenter S, Jardim L, Satishchandra P, Andermann E,
1381 Snead OC, 3rd, Lopes-Cendes I, Tsui LC, Delgado-Escueta AV, Rouleau GA,
1382 Scherer SW. 1998. Mutations in a gene encoding a novel protein tyrosine
1383 phosphatase cause progressive myoclonus epilepsy. *Nat Genet* 20:171-4.
- 1384 39. Gentry MS, Guinovart JJ, Minassian BA, Roach PJ, Serratosa JM. 2018. Lafora
1385 disease offers a unique window into neuronal glycogen metabolism. *J Biol Chem*
1386 293:7117-7125.
- 1387 40. Duran J, Hervera A, Markussen KH, Varea O, Lopez-Soldado I, Sun RC, Del Rio JA,
1388 Gentry MS, Guinovart JJ. 2021. Astrocytic glycogen accumulation drives the
1389 pathophysiology of neurodegeneration in Lafora disease. *Brain* 144:2349-2360.
- 1390 41. Sugi T, Tu V, Ma Y, Tomita T, Weiss LM. 2017. *Toxoplasma gondii* Requires
1391 Glycogen Phosphorylase for Balancing Amylopectin Storage and for Efficient
1392 Production of Brain Cysts. *MBio* 8.
- 1393 42. Cao XZ, Wang JL, Elsheikha HM, Li TT, Sun LX, Liang QL, Zhang ZW, Lin RQ.
1394 2019. Characterization of the Role of Amylo-Alpha-1,6-Glucosidase Protein in the
1395 Infectivity of *Toxoplasma gondii*. *Front Cell Infect Microbiol* 9:418.
- 1396 43. Wang JL, Li TT, Elsheikha HM, Liang QL, Zhang ZW, Wang M, Sibley LD, Zhu XQ.
1397 2022. The protein phosphatase 2A holoenzyme is a key regulator of starch

- 1398 metabolism and bradyzoite differentiation in *Toxoplasma gondii*. Nat Commun
1399 13:7560.
- 1400 44. Zhao M, Yang Y, Shi Y, Chen X, Yang Y, Pan L, Du Z, Sun H, Yao C, Ma G, Du A.
1401 2023. PP2A α -B'/PR61 Holoenzyme of *Toxoplasma gondii* Is Required for
1402 the Amylopectin Metabolism and Proliferation of Tachyzoites. Microbiol Spectr
1403 11:e0010423.
- 1404 45. Gentry MS, Downen RH, 3rd, Worby CA, Mattoo S, Ecker JR, Dixon JE. 2007. The
1405 phosphatase laforin crosses evolutionary boundaries and links carbohydrate
1406 metabolism to neuronal disease. J Cell Biol 178:477-88.
- 1407 46. Gentry MS, Pace RM. 2009. Conservation of the glucan phosphatase laforin is
1408 linked to rates of molecular evolution and the glycogen metabolism of the
1409 organism. BMC Evol Biol 9:138.
- 1410 47. Baba O. 1993. [Production of monoclonal antibody that recognizes glycogen and its
1411 application for immunohistochemistry]. Kokubyo Gakkai Zasshi 60:264-87.
- 1412 48. van de Weerd R, Berbis MA, Sparrius M, Maaskant JJ, Boot M, Paauw NJ, de Vries
1413 N, Boon L, Baba O, Canada FJ, Geurtsen J, Jimenez-Barbero J, Appelmeik BJ.
1414 2015. A murine monoclonal antibody to glycogen: characterization of epitope-fine
1415 specificity by saturation transfer difference (STD) NMR spectroscopy and its use
1416 in mycobacterial capsular alpha-glucan research. Chembiochem 16:977-89.
- 1417 49. Oe Y, Baba O, Ashida H, Nakamura KC, Hirase H. 2016. Glycogen distribution in
1418 the microwave-fixed mouse brain reveals heterogeneous astrocytic patterns. Glia
1419 64:1532-45.

- 1420 50. Skurat AV, Segvich DM, DePaoli-Roach AA, Roach PJ. 2017. Novel method for
1421 detection of glycogen in cells. *Glycobiology* 27:416-424.
- 1422 51. Guimaraes EV, de Carvalho L, Barbosa HS. 2003. An alternative technique to reveal
1423 polysaccharides in *Toxoplasma gondii* tissue cysts. *Mem Inst Oswaldo Cruz*
1424 98:915-7.
- 1425 52. Troublefield CA, Miracle JS, Murphy RD, Donkin RW, Sinai AP. 2023. Factors
1426 Influencing Tissue Cyst Yield in a Murine Model of Chronic Toxoplasmosis. *Infect*
1427 *Immun* 91:e0056622.
- 1428 53. Sidik SM, Hackett CG, Tran F, Westwood NJ, Lourido S. 2014. Efficient genome
1429 engineering of *Toxoplasma gondii* using CRISPR/Cas9. *PLoS One* 9:e100450.
- 1430 54. Fritz HM, Buchholz KR, Chen X, Durbin-Johnson B, Rocke DM, Conrad PA,
1431 Boothroyd JC. 2012. Transcriptomic analysis of toxoplasma development reveals
1432 many novel functions and structures specific to sporozoites and oocysts. *PLoS*
1433 *One* 7:e29998.
- 1434 55. Choi CP, Moon AS, Back PS, Jami-Alahmadi Y, Vashisht AA, Wohlschlegel JA,
1435 Bradley PJ. 2019. A photoactivatable crosslinking system reveals protein
1436 interactions in the *Toxoplasma gondii* inner membrane complex. *PLoS Biol*
1437 17:e3000475.
- 1438 56. Shen B, Brown KM, Lee TD, Sibley LD. 2014. Efficient gene disruption in diverse
1439 strains of *Toxoplasma gondii* using CRISPR/CAS9. *mBio* 5:e01114-14.
- 1440 57. Sidik SM, Huet D, Ganesan SM, Huynh MH, Wang T, Nasamu AS, Thiru P, Saeij
1441 JP, Carruthers VB, Niles JC, Lourido S. 2016. A Genome-wide CRISPR Screen

- 1442 in *Toxoplasma* Identifies Essential Apicomplexan Genes. *Cell* 166:1423-1435
1443 e12.
- 1444 58. Markus BM, Bell GW, Lorenzi HA, Lourido S. 2019. Optimizing Systems for Cas9
1445 Expression in *Toxoplasma gondii*. *mSphere* 4.
- 1446 59. Sun RC, Young LEA, Bruntz RC, Markussen KH, Zhou Z, Conroy LR, Hawkinson
1447 TR, Clarke HA, Stanback AE, Macedo JKA, Emanuelle S, Brewer MK, Rondon
1448 AL, Mestas A, Sanders WC, Mahalingan KK, Tang B, Chikwana VM, Segvich
1449 DM, Contreras CJ, Allenger EJ, Brainson CF, Johnson LA, Taylor RE, Armstrong
1450 DD, Shaffer R, Waechter CJ, Vander Kooi CW, DePaoli-Roach AA, Roach PJ,
1451 Hurley TD, Drake RR, Gentry MS. 2021. Brain glycogen serves as a critical
1452 glucosamine cache required for protein glycosylation. *Cell Metab* 33:1404-1417
1453 e9.
- 1454 60. Brewer MK, Uittenbogaard A, Austin GL, Segvich DM, DePaoli-Roach A, Roach PJ,
1455 McCarthy JJ, Simmons ZR, Brandon JA, Zhou Z, Zeller J, Young LEA, Sun RC,
1456 Pauly JR, Aziz NM, Hodges BL, McKnight TR, Armstrong DD, Gentry MS. 2019.
1457 Targeting Pathogenic Lafora Bodies in Lafora Disease Using an Antibody-
1458 Enzyme Fusion. *Cell Metab* 30:689-705 e6.
- 1459 61. King EFB, Cobbold SA, Uboldi AD, Tonkin CJ, McConville MJ. 2020. Metabolomic
1460 Analysis of *Toxoplasma gondii* Tachyzoites. *Methods Mol Biol* 2071:435-452.
- 1461 62. Nitzsche R, Zagoriy V, Lucius R, Gupta N. 2016. Metabolic Cooperation of Glucose
1462 and Glutamine Is Essential for the Lytic Cycle of Obligate Intracellular Parasite
1463 *Toxoplasma gondii*. *J Biol Chem* 291:126-41.

- 1464 63. Oppenheim RD, Creek DJ, Macrae JI, Modrzynska KK, Pino P, Limenitakis J,
1465 Polonais V, Seeber F, Barrett MP, Billker O, McConville MJ, Soldati-Favre D.
1466 2014. BCKDH: the missing link in apicomplexan mitochondrial metabolism is
1467 required for full virulence of *Toxoplasma gondii* and *Plasmodium berghei*. PLoS
1468 Pathog 10:e1004263.
- 1469 64. Endo T, Sethi KK, Piekarski G. 1982. *Toxoplasma gondii*: calcium ionophore
1470 A23187-mediated exit of trophozoites from infected murine macrophages. Exp
1471 Parasitol 53:179-88.
- 1472 65. Lourido S, Tang K, Sibley LD. 2012. Distinct signalling pathways control *Toxoplasma*
1473 egress and host-cell invasion. EMBO J 31:4524-34.
- 1474 66. Hotchin J, Kinch W, Benson L. 1971. Lytic and turbid plaque-type mutants of
1475 lymphocytic choriomeningitis virus as a cause of neurological disease or
1476 persistent infection. Infect Immun 4:281-6.
- 1477 67. Fiala M. 1968. Plaque formation by 55 rhinovirus serotypes. Appl Microbiol 16:1445-
1478 50.
- 1479 68. Ferguson DJ. 2004. Use of molecular and ultrastructural markers to evaluate stage
1480 conversion of *Toxoplasma gondii* in both the intermediate and definitive host. Int
1481 J Parasitol 34:347-60.
- 1482 69. Sinai AP. 2008. Biogenesis of and activities at the *Toxoplasma gondii*
1483 parasitophorous vacuole membrane. Subcell Biochem 47:155-64.
- 1484 70. Watts EA, Dhara A, Sinai AP. 2017. Purification *Toxoplasma gondii* Tissue Cysts
1485 Using Percoll Gradients. Curr Protoc Microbiol 45:20C 2 1-20C 2 19.

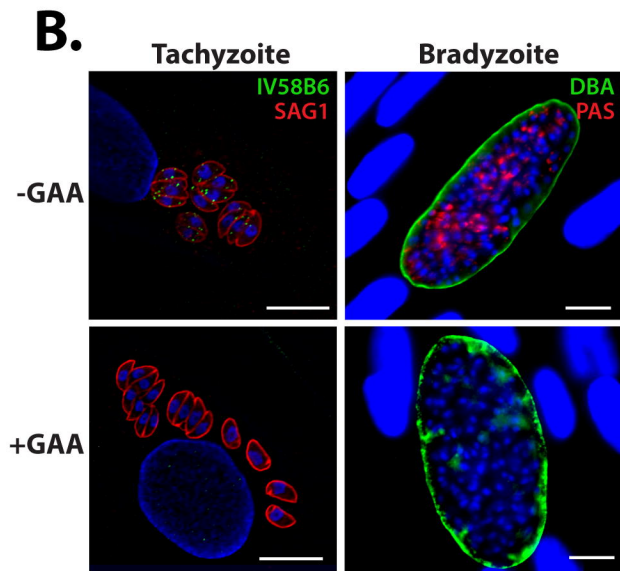
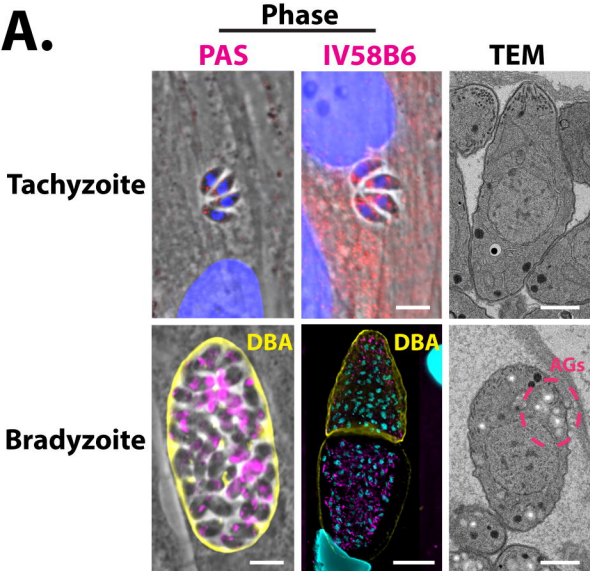
- 1486 71. Kumar S, Ciraolo G, Hinge A, Filippi MD. 2014. An efficient and reproducible
1487 process for transmission electron microscopy (TEM) of rare cell populations. J
1488 Immunol Methods 404:87-90.
- 1489 72. Kumar S, Filippi MD. 2016. An Alternative Approach for Sample Preparation with
1490 Low Cell Number for TEM Analysis. J Vis Exp doi:10.3791/54724.
- 1491 73. Sinai AP, Suvorova ES. 2020. The RESTRICTION checkpoint: a window of
1492 opportunity governing developmental transitions in *Toxoplasma gondii*. Curr Opin
1493 Microbiol 58:99-105.
- 1494 74. Xue Y, Theisen TC, Rastogi S, Ferrel A, Quake SR, Boothroyd JC. 2020. A single-
1495 parasite transcriptional atlas of *Toxoplasma gondii* reveals novel control of
1496 antigen expression. Elife 9.
- 1497 75. Olson WJ, Martorelli Di Genova B, Gallego-Lopez G, Dawson AR, Stevenson D,
1498 Amador-Noguez D, Knoll LJ. 2020. Dual metabolomic profiling uncovers
1499 Toxoplasma manipulation of the host metabolome and the discovery of a novel
1500 parasite metabolic capability. PLoS Pathog 16:e1008432.
- 1501 76. Zeeman SC, Delatte T, Messerli G, Umhang M, Stettler M, Mettler T, Streb S,
1502 Reinhold H, Kotting O. 2007. Starch breakdown: recent discoveries suggest
1503 distinct pathways and novel mechanisms. Funct Plant Biol 34:465-473.
- 1504 77. Zeeman SC, Smith SM, Smith AM. 2007. The diurnal metabolism of leaf starch.
1505 Biochem J 401:13-28.
- 1506 78. Mahlow S, Orzechowski S, Fettke J. 2016. Starch phosphorylation: insights and
1507 perspectives. Cell Mol Life Sci 73:2753-64.

- 1508 79. Ferguson DJ, Hutchison WM. 1987. An ultrastructural study of the early
1509 development and tissue cyst formation of *Toxoplasma gondii* in the brains of
1510 mice. *Parasitol Res* 73:483-91.
- 1511 80. Niittyla T, Comparot-Moss S, Lue WL, Messerli G, Trevisan M, Seymour MD,
1512 Gatehouse JA, Villadsen D, Smith SM, Chen J, Zeeman SC, Smith AM. 2006.
1513 Similar protein phosphatases control starch metabolism in plants and glycogen
1514 metabolism in mammals. *J Biol Chem* 281:11815-8.
- 1515 81. Zeeman SC, Northrop F, Smith AM, Rees T. 1998. A starch-accumulating mutant of
1516 *Arabidopsis thaliana* deficient in a chloroplastic starch-hydrolysing enzyme. *Plant*
1517 *J* 15:357-65.
- 1518 82. Shukla A, Olszewski KL, Llinas M, Rommereim LM, Fox BA, Bzik DJ, Xia D,
1519 Wastling J, Beiting D, Roos DS, Shanmugam D. 2018. Glycolysis is important for
1520 optimal asexual growth and formation of mature tissue cysts by *Toxoplasma*
1521 *gondii*. *Int J Parasitol* 48:955-968.
- 1522 83. Blume M, Rodriguez-Contreras D, Landfear S, Fleige T, Soldati-Favre D, Lucius R,
1523 Gupta N. 2009. Host-derived glucose and its transporter in the obligate
1524 intracellular pathogen *Toxoplasma gondii* are dispensable by glutaminolysis.
1525 *Proc Natl Acad Sci U S A* 106:12998-3003.
- 1526 84. Dubey R, Staker BL, Foe IT, Bogyo M, Myler PJ, Ngo HM, Gubbels MJ. 2017.
1527 Membrane skeletal association and post-translational allosteric regulation of
1528 *Toxoplasma gondii* GAPDH1. *Mol Microbiol* 103:618-634.

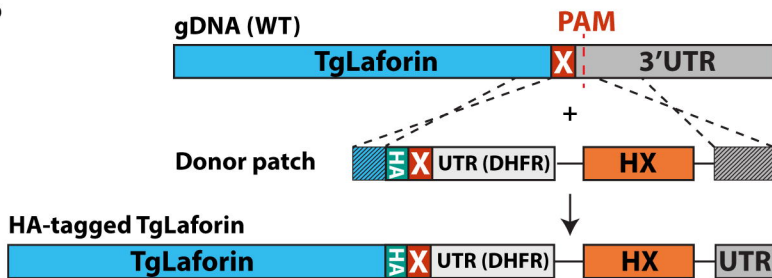
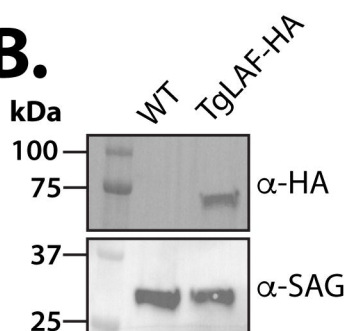
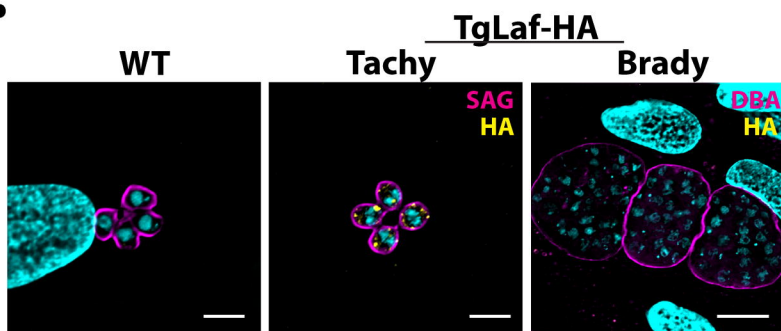
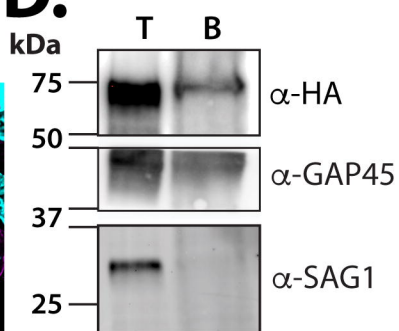
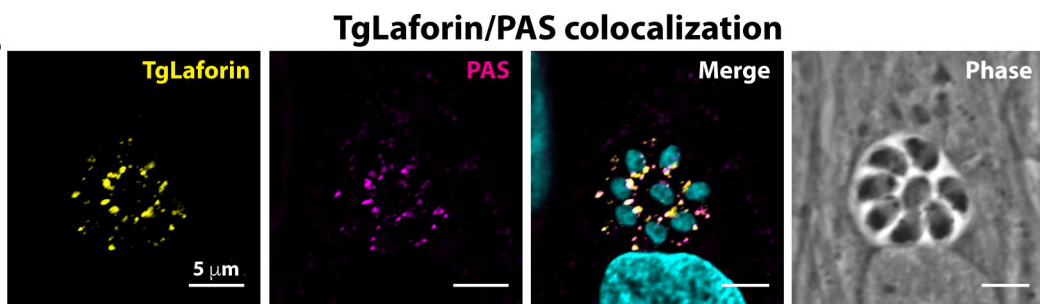
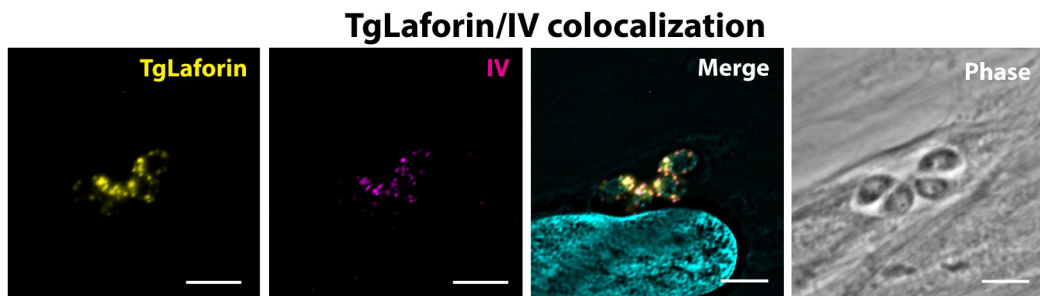
- 1529 85. Xia N, Ye S, Liang X, Chen P, Zhou Y, Fang R, Zhao J, Gupta N, Yang S, Yuan J,
1530 Shen B. 2019. Pyruvate Homeostasis as a Determinant of Parasite Growth and
1531 Metabolic Plasticity in *Toxoplasma gondii*. mBio 10.
- 1532 86. Suresh K, Mak JW, Yong HS. 1991. Immune response in acute *Toxoplasma*
1533 infection of Balb/C, ICR and CBA/J mice. Southeast Asian J Trop Med Public
1534 Health 22:452-4.
- 1535 87. Araujo FG, Huskinson-Mark J, Gutteridge WE, Remington JS. 1992. In vitro and in
1536 vivo activities of the hydroxynaphthoquinone 566C80 against the cyst form of
1537 *Toxoplasma gondii*. Antimicrob Agents Chemother 36:326-30.
- 1538 88. Araujo FG, Lin T, Remington JS. 1993. The activity of atovaquone (566C80) in
1539 murine toxoplasmosis is markedly augmented when used in combination with
1540 pyrimethamine or sulfadiazine. J Infect Dis 167:494-7.
- 1541 89. Doggett JS, Nilsen A, Forquer I, Wegmann KW, Jones-Brando L, Yolken RH,
1542 Bordon C, Charman SA, Katneni K, Schultz T, Burrows JN, Hinrichs DJ, Meunier
1543 B, Carruthers VB, Riscoe MK. 2012. Endochin-like quinolones are highly
1544 efficacious against acute and latent experimental toxoplasmosis. Proc Natl Acad
1545 Sci U S A 109:15936-41.
- 1546 90. Doggett JS, Schultz T, Miller AJ, Bruzual I, Pou S, Winter R, Dodean R, Zakharov
1547 LN, Nilsen A, Riscoe MK, Carruthers VB. 2020. Orally Bioavailable Endochin-
1548 Like Quinolone Carbonate Ester Prodrug Reduces *Toxoplasma gondii* Brain
1549 Cysts. Antimicrob Agents Chemother 64.
- 1550 91. Vidadala RS, Rivas KL, Ojo KK, Hulverson MA, Zambriski JA, Bruzual I, Schultz TL,
1551 Huang W, Zhang Z, Scheele S, DeRocher AE, Choi R, Barrett LK, Siddaramaiah

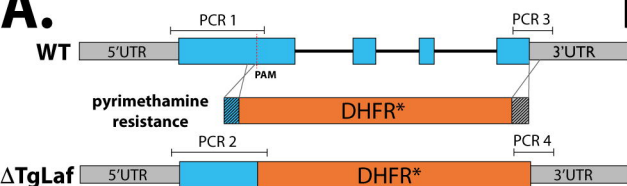
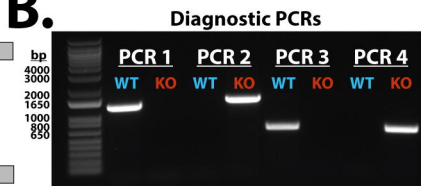
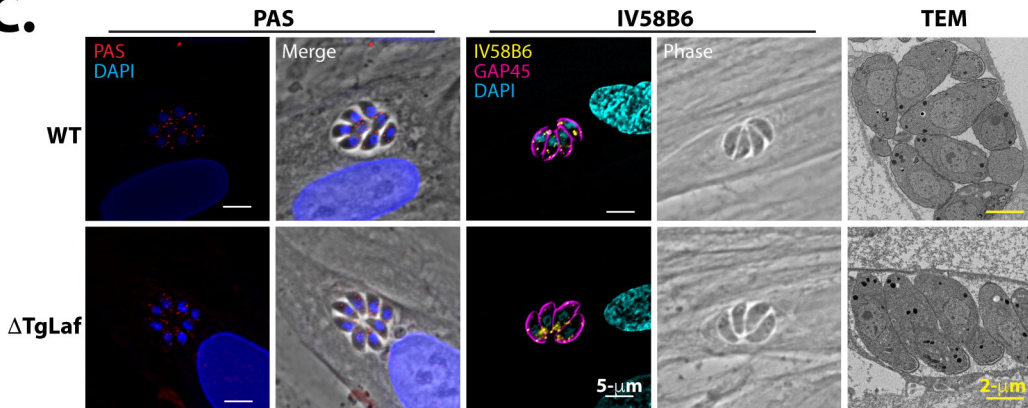
- 1552 LK, Hol WG, Fan E, Merritt EA, Parsons M, Freiberg G, Marsh K, Kempf DJ,
1553 Carruthers VB, Isoherranen N, Doggett JS, Van Voorhis WC, Maly DJ. 2016.
1554 Development of an Orally Available and Central Nervous System (CNS)
1555 Penetrant *Toxoplasma gondii* Calcium-Dependent Protein Kinase 1 (TgCDPK1)
1556 Inhibitor with Minimal Human Ether-a-go-go-Related Gene (hERG) Activity for
1557 the Treatment of Toxoplasmosis. *J Med Chem* 59:6531-46.
- 1558 92. McPhillie MJ, Zhou Y, Hickman MR, Gordon JA, Weber CR, Li Q, Lee PJ,
1559 Amporndanai K, Johnson RM, Darby H, Woods S, Li ZH, Priestley RS, Ristroph
1560 KD, Biering SB, El Bissati K, Hwang S, Hakim FE, Dovgin SM, Lykins JD,
1561 Roberts L, Hargrave K, Cong H, Sinai AP, Muench SP, Dubey JP, Prud'homme
1562 RK, Lorenzi HA, Biagini GA, Moreno SN, Roberts CW, Antonyuk SV, Fishwick
1563 CWG, McLeod R. 2020. Potent Tetrahydroquinolone Eliminates Apicomplexan
1564 Parasites. *Front Cell Infect Microbiol* 10:203.
- 1565 93. Brown KM, Long S, Sibley LD. 2018. Conditional Knockdown of Proteins Using
1566 Auxin-inducible Degron (AID) Fusions in *Toxoplasma gondii*. *Bio Protoc* 8.
- 1567 94. Bolte S, Cordelieres FP. 2006. A guided tour into subcellular colocalization analysis
1568 in light microscopy. *J Microsc* 224:213-32.
- 1569 95. Mayoral J, Di Cristina M, Carruthers VB, Weiss LM. 2020. *Toxoplasma gondii*:
1570 Bradyzoite Differentiation In Vitro and In Vivo. *Methods Mol Biol* 2071:269-282.
- 1571 96. Schindelin J, Arganda-Carreras I, Frise E, Kaynig V, Longair M, Pietzsch T,
1572 Preibisch S, Rueden C, Saalfeld S, Schmid B, Tinevez JY, White DJ, Hartenstein
1573 V, Eliceiri K, Tomancak P, Cardona A. 2012. Fiji: an open-source platform for
1574 biological-image analysis. *Nat Methods* 9:676-82.

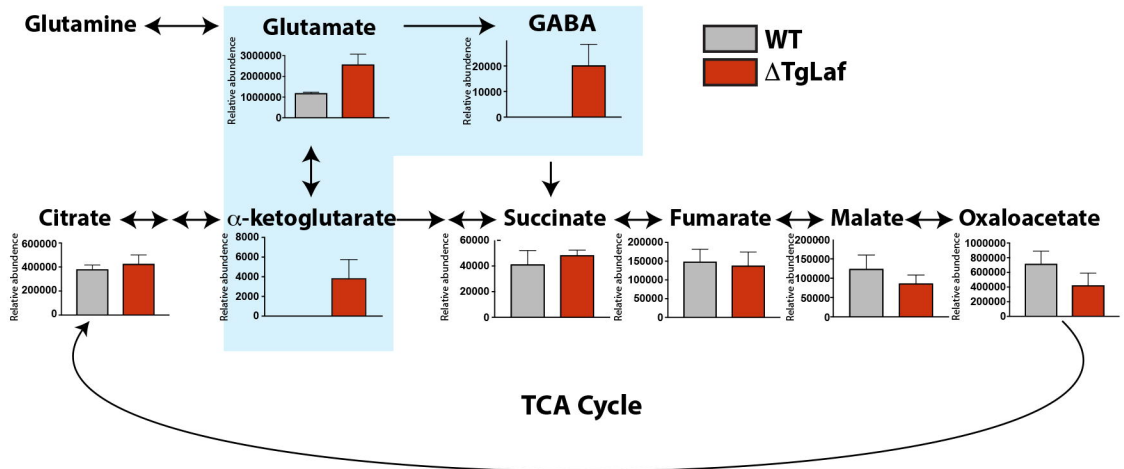
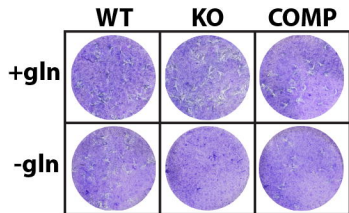
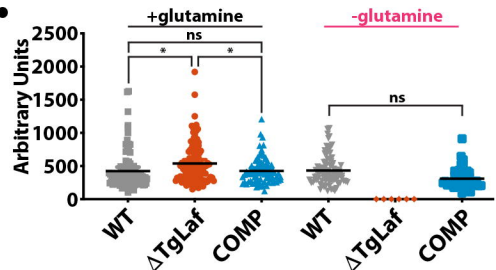
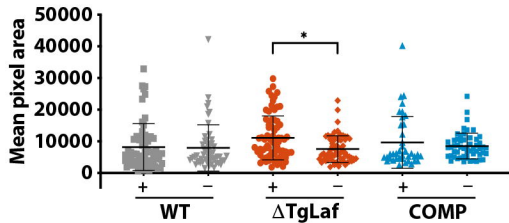
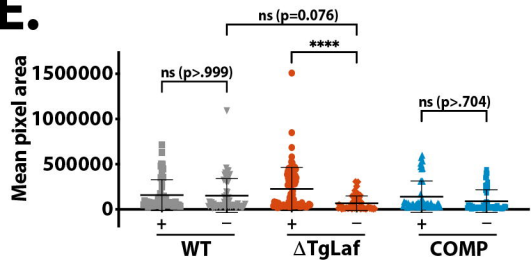
- 1575 97. Sinai AP, Webster P, Joiner KA. 1997. Association of host cell endoplasmic
1576 reticulum and mitochondria with the *Toxoplasma gondii* parasitophorous vacuole
1577 membrane: a high affinity interaction. J Cell Sci 110 (Pt 17):2117-28.
- 1578 98. Andres DA, Young LEA, Veeranki S, Hawkinson TR, Levitan BM, He D, Wang C,
1579 Satin J, Sun RC. 2020. Improved workflow for mass spectrometry-based
1580 metabolomics analysis of the heart. J Biol Chem 295:2676-2686.
- 1581 99. Markus BM, Bell GW, Lorenzi HA, Lourido S. 2019. Optimizing systems for Cas9
1582 expression in *Toxoplasma gondii*. MSphere 4:e00386-19.
- 1583

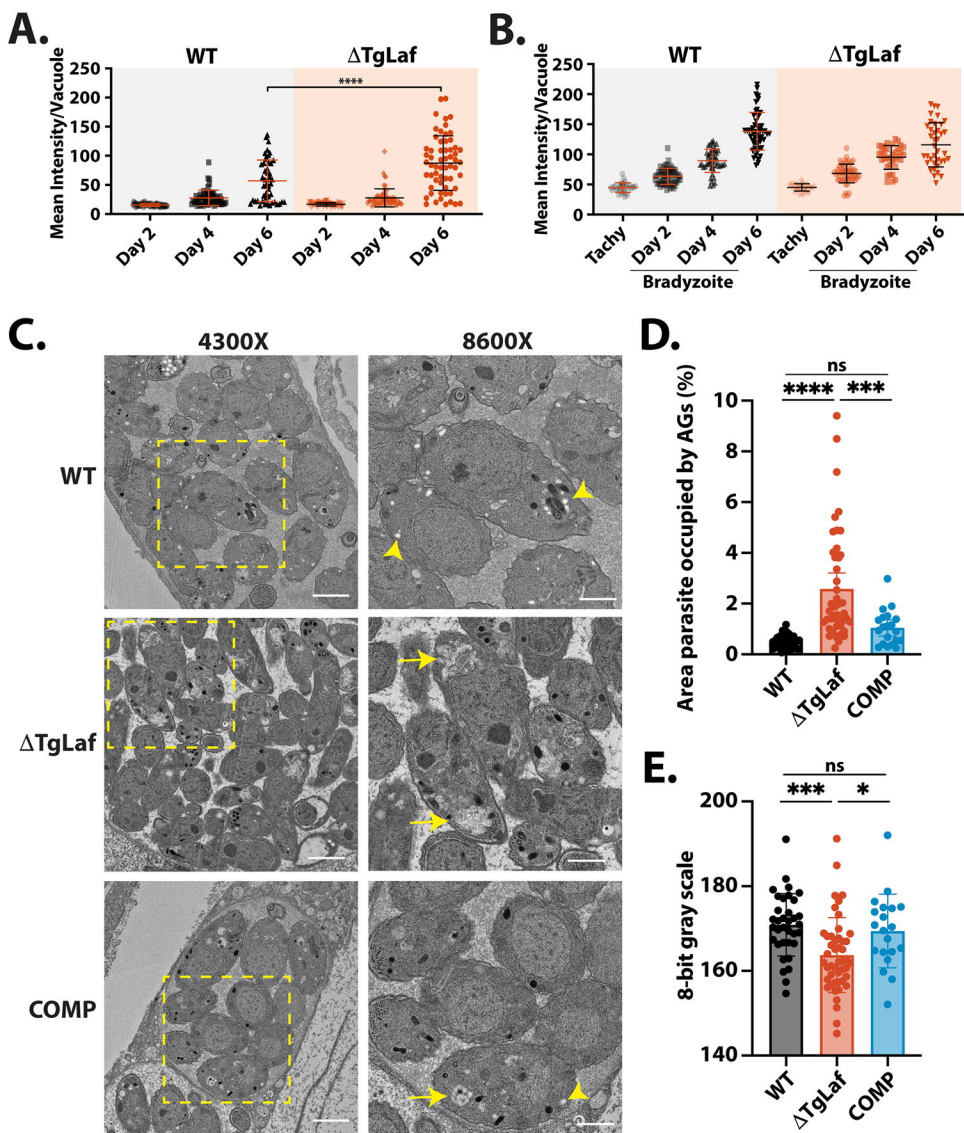


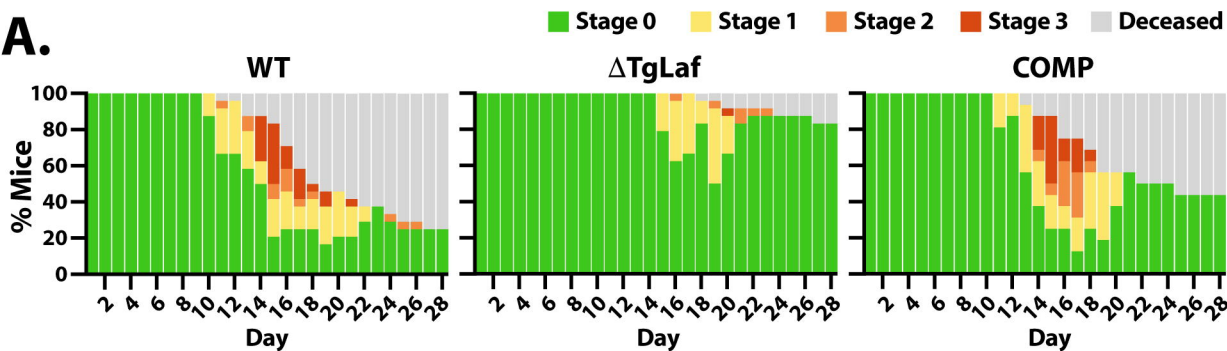
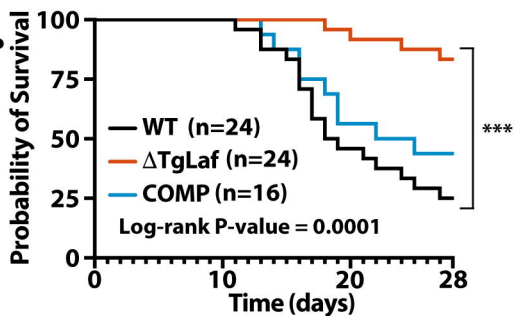
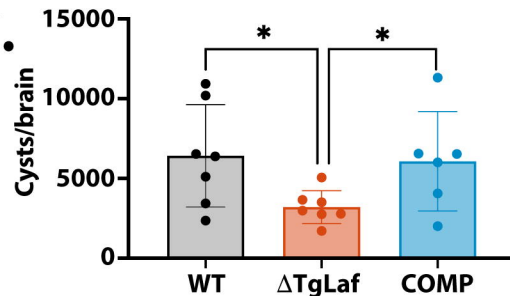
Murphy et al. 2024 Figure 1

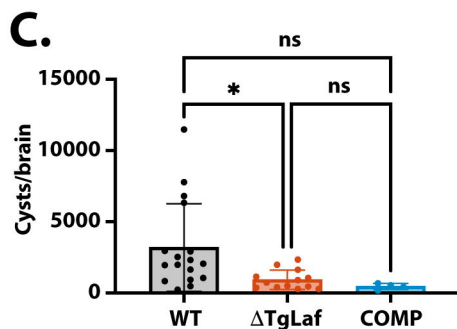
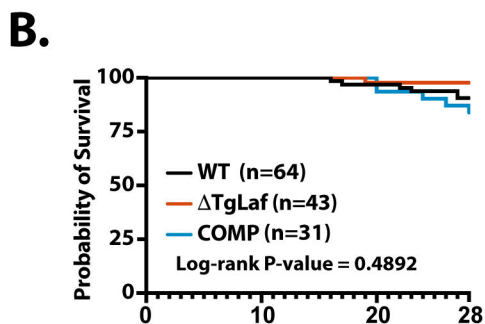
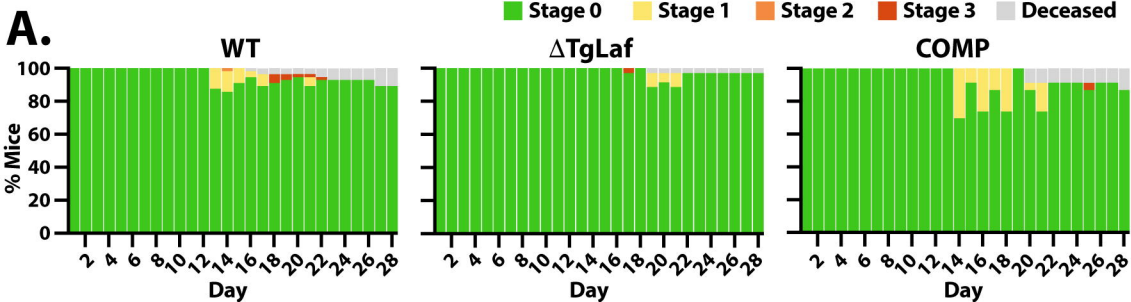
A.**B.****C.****D.****E.****F.**

A.**B.****C.**

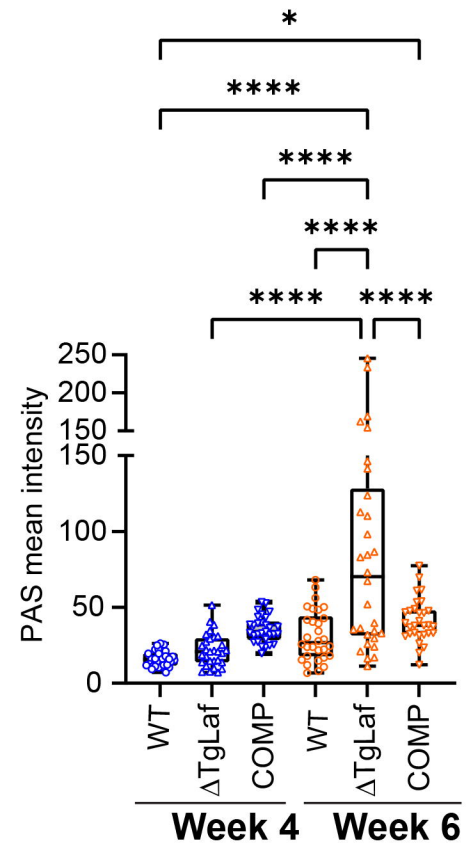
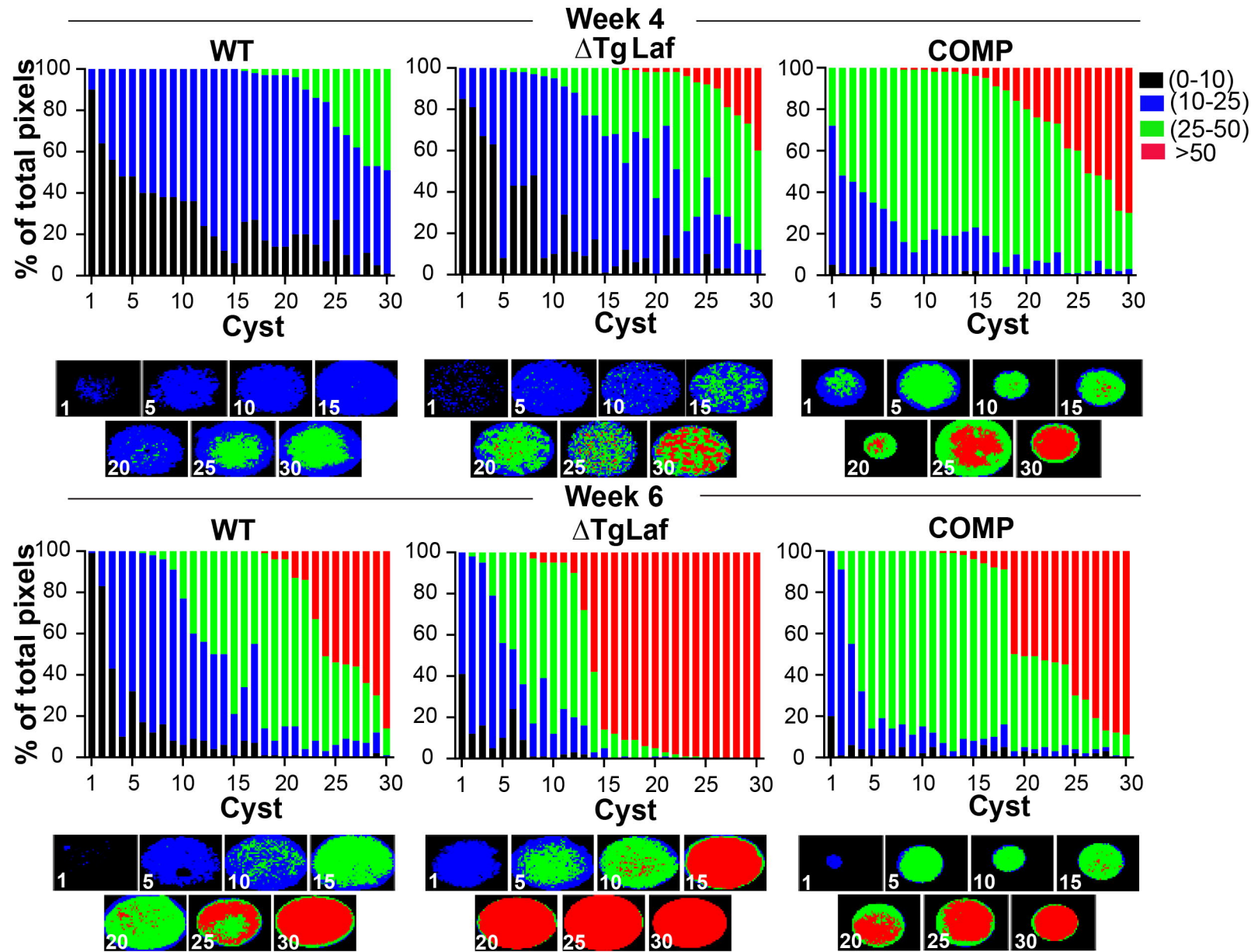
A.**B.****C.****D.****E.**



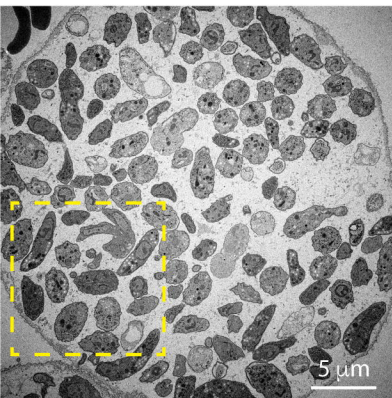
A.**B.****C.**



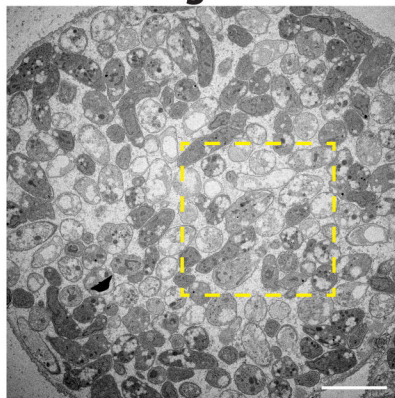
Murphy et al. 2024 Figure 7

A.**B.**

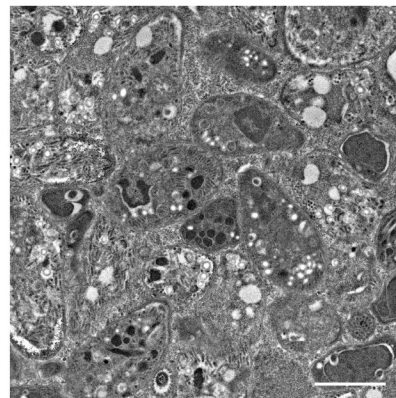
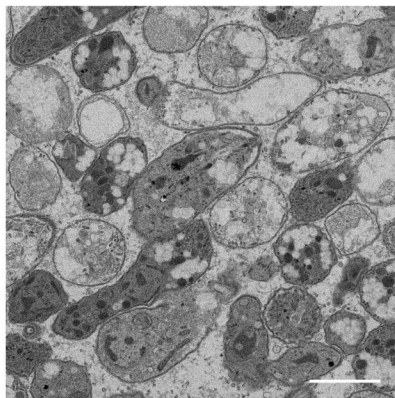
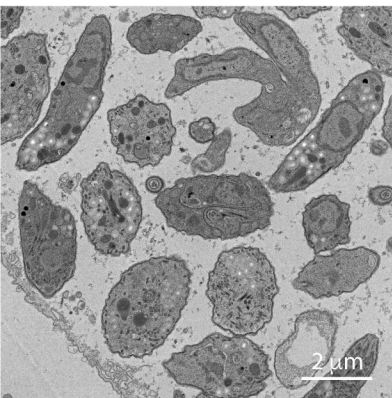
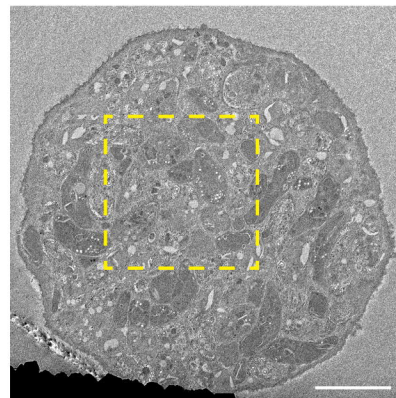
WT



Δ TgLaf



COMP



Murphy et al. 2024 Figure 9